JGR Solid Earth

RESEARCH ARTICLE
10.1029/2022JB025879

Special Section:
Understanding and anticipating Induced Seismicity: from mechanics to seismology

Characterizing Seismogenic Fault Structures of the Lake Pertusillo Reservoir Induced Seismicity (Southern Italy) Using a Relocated Template-Matching Catalog

L. Valoroso[1], D. Piccinini[2], L. Improta[1], S. Gaviano[2,3], and C. Giunchi[2]

[1]Osservatorio Nazionale Terremoti, Istituto Nazionale di Geofisica e Vulcanologia, Roma, Italy, [2]Istituto Nazionale di Geofisica e Vulcanologia, Sezione di Pisa, Pisa, Italy, [3]Università degli Studi di Firenze, Firenze, Italy

Key Points:

- We use template-matching to build an enhanced catalog of 5k earthquakes describing the Pertusillo reservoir induced seismicity
- Seismicity is organized in four clusters featuring different *b-value* and confined in an aqueous carbonate reservoir
- Seismicity reactivates, in extension, inherited reverse faults and it is controlled by the physical properties of the fractured carbonates

Supporting Information:

Supporting Information may be found in the online version of this article.

Correspondence to:

L. Valoroso,
luisa.valoroso@ingv.it

Citation:

Valoroso, L., Piccinini, D., Improta, L., Gaviano, S., & Giunchi, C. (2023). Characterizing seismogenic fault structures of the Lake Pertusillo reservoir induced seismicity (Southern Italy) using a relocated template-matching catalog. *Journal of Geophysical Research: Solid Earth*, *128*, e2022JB025879. https://doi.org/10.1029/2022JB025879

Received 21 OCT 2022
Accepted 11 JUN 2023

Author Contributions:

Conceptualization: L. Valoroso, D. Piccinini, L. Improta, C. Giunchi
Data curation: L. Valoroso, S. Gaviano, C. Giunchi
Formal analysis: L. Valoroso, D. Piccinini, L. Improta

Abstract We present a detailed analysis of the small magnitude ($M_L < 3$) Reservoir Induced Seismicity associated with the Pertusillo water reservoir located in the high seismic hazard zone of Val d'Agri (Southern Italy). We apply template-matching detection to a 13-month-long dense passive survey, obtaining a final high-precision double-difference catalog of 5,070 earthquakes ($-0.7 < M_L < 2.6$, $M_C = 0.2$). The new catalog allows precisely tracking the spatiotemporal distribution of the swarm-seismicity and to map the *b-value* of the Gutenberg-Richter law. We combine seismicity data with available subsurface geophysical data, fostering an improved interpretation of the induced seismicity. We identify four seismicity-clusters showing rapid changes in seismic rate which correlate to severe seasonal oscillations. Seismicity unravels new km-scale faults or better define faults partially-illuminated by *template* earthquakes. *b-value* shows a significant spatial variability, with very-high *b-value* (up to 2) within areas of distributed seismicity and lower (~1.3) *b-value* for on-fault seismicity featuring larger magnitude events. Seismicity is confined within a brine-saturated fractured carbonate reservoir, while earthquake distribution and rate are controlled by the fault architecture and rock properties (e.g., inherited fluid pathways, rock fracturing, pore fluid pressure). In particular, most earthquakes reactivate, with extensional kinematics, pre-existing reverse/transpressional faults favorably oriented in the present-day extension. All observations suggest that a poroelastic stress transmission mechanism, due to the seasonal water level oscillation, can explain the Pertusillo lake seismicity. This study confirms the importance of investigating the complex interaction among stress changes caused by human activities, pre-existing faults and local stress field to correctly assess the hazard posed by induced seismicity.

Plain Language Summary The Val d'Agri basin in Southern Italy is characterized by a high seismic hazard as evidenced by the strong 1857 M7.1 earthquake, whose causative fault is still debated. The area is also a natural laboratory for studying anthropogenic seismicity since it hosts two well-documented cases of seismicity induced by: (a) the exploitation of a giant oilfield with a clear case of wastewater injection-induced-seismicity and (b) the seasonal water level oscillation in the medium-size Pertusillo water reservoir (PWR). We focus on the reservoir induced seismicity to better understand the physical mechanism behind its genesis and time-space evolution. We applied a technique that allows us to extract smaller earthquakes from known ones (*templates*), increasing 10-times the original catalog and helping to better characterize the spatiotemporal seismicity behavior. Seismicity is organized in four distinct clusters activated in response to the seasonal loading/unloading phases of the PWR. It delineates km-scale faults and is confined within highly fractured aqueous carbonates. Our results furnish new data to understand how the stress induced by the lake level changes influences seismicity nucleation in this hazardous area, spurring for a more accurate estimation of the seismic hazard of the area.

1. Introduction

The Val d'Agri basin in the southern Apennines seismic belt is one of the central Mediterranean regions with the highest seismogenic potential, as testified by the strongest peninsular 1857 M7.1 Basilicata earthquake (Mallet, 1862; Rovida & Antonucci, 2021). In the past 40 years, the Val d'Agri experienced weak background seismicity seldom exceeding M3. Background activity coexists with two well-documented cases of induced seismicity associated to: (a) the exploitation of a giant oilfield with a clear case of wastewater injection induced seismicity (Improta et al., 2015) and (b) the medium-sized Pertusillo water reservoir (PWR). Local seismic stations installed since 2002 recorded repeated weak swarms to the southwest of the PWR, which strictly relate

Funding acquisition: L. Valoroso
Investigation: L. Valoroso, L. Improta
Methodology: L. Valoroso, D. Piccinini, L. Improta, S. Gaviano, C. Giunchi
Software: S. Gaviano, C. Giunchi
Supervision: L. Improta
Writing – original draft: L. Valoroso, D. Piccinini, L. Improta

to seasonal water oscillations as high as 25 m (Figures 1b–1d), corresponding to storage changes as large as 120 million m^3. This spatiotemporal correlation led Valoroso et al. (2009) and Stabile et al. (2014) to interpret the Pertusillo lake earthquakes as protracted RIS (the reservoir impoundment dates back to 1962), a conclusion confirmed by statistical assessments (Telesca et al., 2015). This type of Reservoir Induced Seismicity (RIS) mostly depends on the frequency and amplitude of lake-level changes and on the hydromechanical properties of the crust (Talwani, 1997). While a detailed model of the injection-induced earthquakes occurring in the oilfield has been proposed recently (Hager et al., 2021; Improta et al., 2017), the physical mechanism behind the PWR seismicity and its relation to fault structures are still poorly understood.

Protracted RIS can be associated with destructive M6+ earthquakes, as documented by the Konya reservoir seismicity in India (Talwani, 1997). Worldwide cases of M4+ RIS earthquakes have rapidly increased in recent years (Gupta, 2022 and references therein) focusing the attention of the seismological community to better understand the physical mechanism and hazard posed by seismicity related to water reservoirs. Even if the PWR seismicity is characterized by low energy with largest events around M_L3, a deeper understanding is compelling due to the presence of active faults, potential source of M6+ earthquakes close to the lake (Improta et al., 2010), in an area where the source of the large M7.1, 1857 Basilicata earthquake is still debated (Bello et al., 2022; DISS Working Group, 2021).

Here, we study the PWR induced seismicity through a very-high resolution earthquake catalog computed by applying *template-matching* (TM) detection techniques to seismic data recorded during a 1-year-long dense passive survey. TM uses cross-correlation (CC) between continuous seismic data and known earthquake recordings (*templates*) to detect previously unidentified events in continuous data. This method has proven very effective compared to traditional techniques (e.g., Short Time Average (STA)/Long Time Average (LTA)), especially in areas characterized by dense clusters of small-magnitude seismic events (e.g., Shearer, 1994; Shelly et al., 2016; Ross et al., 2019; Cochran et al., 2018). Enhanced TM catalogs have low completeness magnitude (M_C) allowing to image the geometry of faults and to furnish details of the seismicity pattern; also, they allow to investigate the *b-value* of the frequency-magnitude distribution (FMD), a key parameter to map stress distribution in the subsurface structure. This parameter shows a wide range of values worldwide, depending for example, on the tectonic stress (Amitrano, 2003; Scholz, 2015; Schorlemmer et al., 2005; Spada et al., 2013) or depth (Amorèse et al., 2010). In particular, low *b-value* seems to pinpoint highly stressed portions of the crust such as fault asperities (De Gori et al., 2012; Sugan et al., 2014).

We present a high-quality catalog of 5,070 earthquakes ($-0.75 < M_L < 2.6$ and $M_C = 0.2$) computed by combining detailed *TM* detection and high-precision double-difference location techniques (Figure 2). The new catalog allows us to precisely track the spatiotemporal distribution of clustered seismicity, to pinpoint the activated faults, and to map spatial variations of the *b-value*. Also, we use subsurface information on physical and hydraulic properties of the crust in the survey area to improve our understanding of the physical mechanism behind the seismicity induced by level oscillation of the PWR.

2. Geologic and Seismotectonic Outline

The NW-trending Val d'Agri Quaternary basin is located in the NW-trending E-verging southern Apennine fold-and-thrust orogenic belt, originated by the convergence between the African and European plates (Patacca and Scandone, 1989). The upper crustal structure (Candela et al., 2015 and references therein) is dominated by a NW-trending E-verging thrust-and-fold system that deforms Meso-Cenozoic carbonate platform and basin sequences developed during Miocene—Early Pleistocene shortening. The belt is structured into two main units (Figures 1a and 1c): (a) a shallow stack of 2–3 km thick rootless nappes including carbonate platform and deep pelagic sequences (Triassic—Miocene) covered by thick flysch sequences (Upper Miocene—Pliocene); (b) a 5–7 km thick platform carbonate sequence (Triassic—Miocene) deformed during Late Pliocene—Early Pleistocene by SW-dipping steep thrust faults with associated wide ramp anticlines and flower structures (i.e., Inner Apulia Platform). The rootless nappes are separated by the underlying Apulian carbonates through a thick tectonic mélange consisting of Miocene—Lower Pliocene deeply deformed foredeep deposits (Mazzoli et al., 2001; Shiner et al., 2004). Low-porosity, fractured Miocene-Jurassic limestone and dolomite of the Apulia Platform form the local reservoir rocks. The Val d'Agri oilfield extends beneath the Quaternary basin and the eastern ridge (Figures 1a and 1c). Hydrocarbons and formation waters (brines) are extracted from a series of NW-SE trending anticlines developed in the hanging-wall of steep-to-moderately dipping blind fore-thrusts and back-thrusts. The

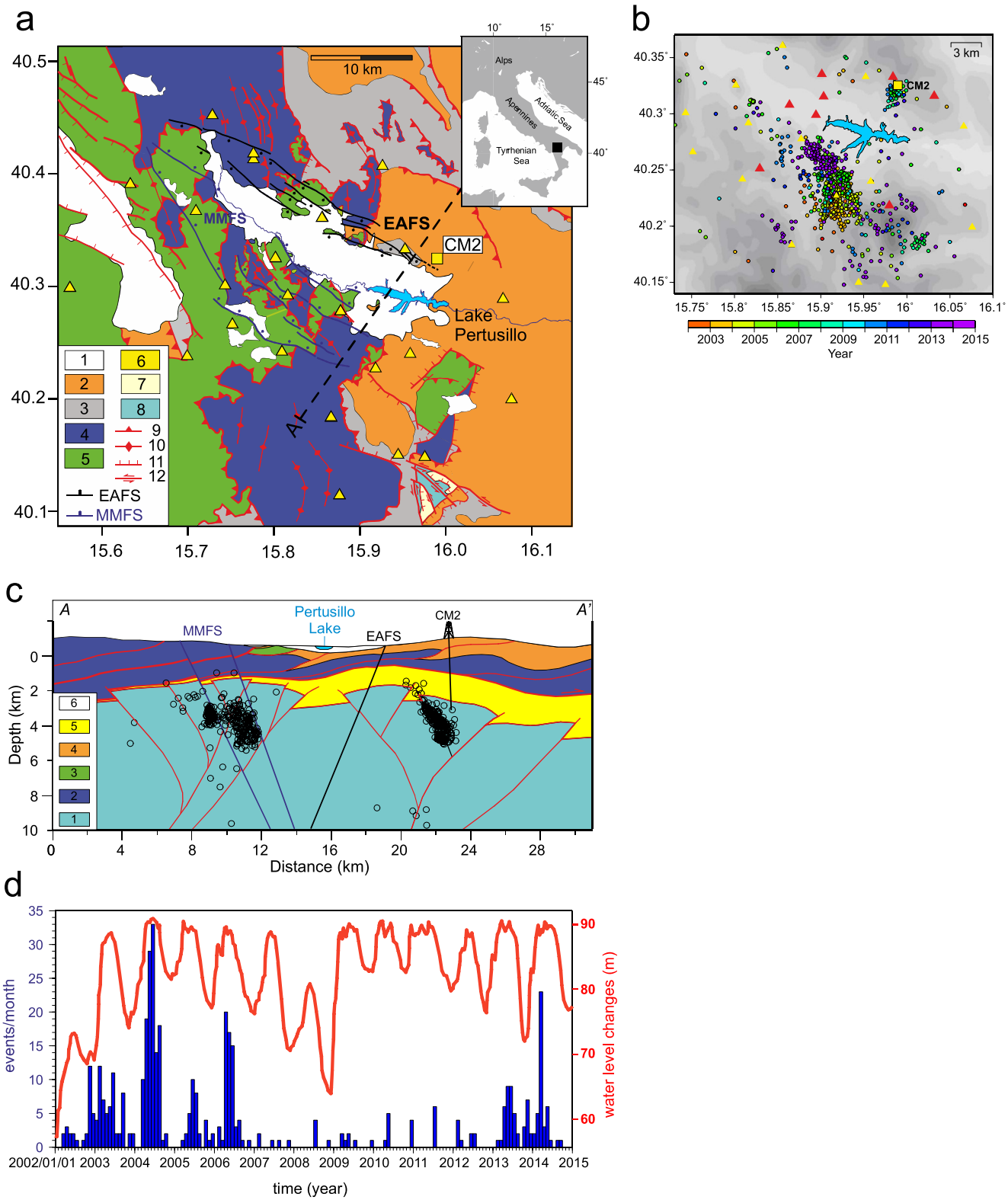

Figure 1.

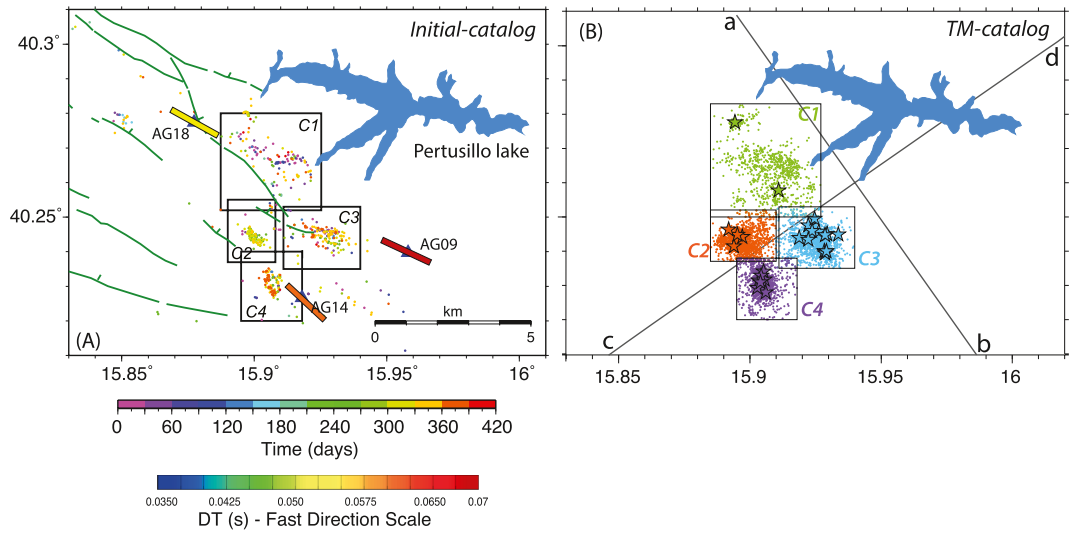

Figure 2. (a) Map distribution of the double-difference *initial-relocated-catalog* (502 earthquakes located to the SW of the Pertusillo lake). Events are color-coded to show the temporal evolution. The four insets indicate the spatial distribution of the *C1–C4* clusters of seismicity (see text for explanation). Blue triangles (AG09, AG14, AG18) are seismic stations of the 2005–2006 Istituto Nazionale di Geofisica e Vulcanologia temporary network used in this study. For these stations, thick lines show the orientation of the maximum horizontal stress (Shmax) inferred from *S*-wave splitting analysis (redrawn from Pastori et al., 2015). (b) Map distribution of the 5,070 earthquakes of the *template-matching* catalog (*TM-catalog*). Colors indicate different clusters, while stars represent $M_L > 1.5$ events. The two black lines indicate the two vertical cross-sections used to map spatiotemporal seismicity distribution in Figure 7.

western boundary of the oilfield corresponds to a main NW-SE striking, NE-dipping back-thrust (Figure 1c) (Hager et al., 2021). This fault separates the hydrocarbon reservoir from a wide Apulian carbonate anticline to the west. This western antiformal structure, referred to as Castellana Structural Trend (Pugliese et al., 2011), relates to a system of blind thrusts and back-thrusts that strikes NW-SE to the southwest of the Val d'Agri basin, and it hosts a 3–4-km-thick aqueous reservoir. The cap rocks of the hydrocarbon and aqueous reservoirs consist of Pliocene clays that stratigraphically cover the Apulian carbonates and of ductile and overpressured tectonic mélange (D'Adda et al., 2018; Mazzoli et al., 2001). The thickness of the mélange unit is extremely variable: more than 1 km in the southern part of the basin, where the oilfield and the PWR are located (Buttinelli et al., 2016), to less than 100 m to the southwest of the basin where the RIS occurs (La Bruna et al., 2018). Subsurface exploration data, the geochemical signature of reservoir fluids, well pressures and oilfield production data indicate that the Val d'Agri hydrocarbon reservoir and the Castellana Trend aqueous reservoir are hydraulically separated. Due to the reservoir compartmentalization, pore pressure perturbations caused by fluid withdrawal and injection cannot propagate from the productive zones of the hydrocarbon reservoir, located to the northeast of the Pertusillo lake, to the southwestern aqueous reservoir of the Castellana Trend where the RIS occurs (Rinaldi et al., 2020).

Figure 1. (a) Geologic map of the Val d'Agri and surrounding regions, based on published data (La Bruna et al., 2018; Maschio et al., 2005). 1. Quaternary continental deposits; 2. Terrigenous sediments of satellite basins (Middle Miocene—Pliocene); 3. Pelagic and slope successions (Cretaceous—Lower Miocene); 4. Mesozoic rocks of the Lagonegro Basin (cherty limestones, cherts and claystones); 5. Western Carbonate Platform (Mesozoic); 6. Tectonic mélange (Miocene—Lower Pliocene); 7. Terrigenous deposits covering the Apulian Platform (Messinian foreland basin sequences); 8. Inner Apulia Platform (Mesozoic—Miocene); 9. reverse faults and overthrusts; 10. Antiform axis; 11. Normal faults; 12. Strike-slip faults; EAFS, Eastern Agri Fault System; MMFS, Mts. Maddalena Fault System. Yellow triangles are temporary stations of the 2005–2006 survey used in this study. The yellow square is the injection well Costa Molina 2 (CM2). A–A′ trace is the geologic section shown in panel (c). (b) Seismicity recorded in the southern sector of the Val d'Agri and close to the Pertusillo Lake from 2002 to 2014 by stations of Istituto Nazionale di Geofisica e Vulcanologia and of the oilfield monitoring network. Earthquake locations are extracted from the catalog of Improta et al. (2017). Only events above the completeness magnitude $M_C = 1.1$ and hypocentral depth <7 km are plotted. Yellow triangles are stations of the 2005–2006 survey (Valoroso et al., 2009), while red triangles are those operated by ENI company. The yellow square is the wastewater injection well CM2. (c) Schematic geological cross-section across the southern sector of the Val d'Agri, based on published data (Maschio et al., 2005; Mazzoli et al., 2013; Van Dijk et al., 2000). 1. Apulian Carbonate Platform; 2. Meso-Cenozoic basin and pelagic sequences; 3. Western Carbonate Platform; 4. Tectonic Mélange; 5. Mio-Pliocene terrigenous sequences; 6. Quaternary deposits of the Val d'Agri. Red lines denote reverse faults and overthrusts, blue and black thick lines are Quaternary normal faults (Monti della Maddalena and Eastern Agri fault systems). Black empty dots are seismic events mainly related to the Pertusillo Lake and CM2 injection-well extracted from the 2002–2014 catalog of Improta et al. (2017). (d) The Pertusillo Lake water level changes are compared with the monthly number of earthquakes that occurred in the region between 2002 and 2014 (longitude 15.87–15.95; latitude 40.20–40.29). Earthquakes are extracted from the catalog of Improta et al. (2017). Only events above the completeness magnitude $M_L \geq 1.1$ and hypocentral depth <7 km are plotted.

This structural setting is complicated by transpressive structures that segment the Apulian thrust-fold structures (D'Adda et al., 2018) and by NW-SE striking extensional fault systems developed since the Middle Pleistocene during the NE-oriented regional extension. The deformation rate is about 3–5 mm/year (Ferranti et al., 2014). The main normal fault systems bounding both sides of the Quaternary basin are (Figures 1a and 1c): the SW-dipping Eastern Agri Fault System to the north-east and the NE-dipping Monti della Maddalena Fault System to the south-west (Cello et al., 2003; Maschio et al., 2005). Both systems consist of arrays of minor segments, possibly indicating fault-immaturity. The accurate geometry at depth and the seismogenic potential of these structures are still debated. Some authors (DISS Working Group, 2021; Ferranti et al., 2014; Improta et al., 2010; Maschio et al., 2005) consider the Monti della Maddalena Fault System as the main structure accommodating the present-day deformation and potential source of M6+ earthquakes. Other authors (Bello et al., 2022 and reference therein) prefer the morphologically evident Eastern Agri Fault System as the main seismogenic structure of the area.

The Val d'Agri experienced only weak earthquakes in the last 40 years, seldom reaching M3. The background seismicity has been monitored with increasing detail since 2002 when a trigger-mode local network run by ENI oil company was deployed. Six additional permanent stations were installed by the Istituto Nazionale di Geofisica e Vulcanologia (INGV) between 2004 and 2006 (Figure 1b). Finally, the higher quality data analyzed in this paper were collected during a dense passive survey we carried out in 2005–2006 in the whole Val d'Agri (Valoroso et al., 2009, 2023a, 2023b). So far, the more complete picture of the local seismicity relies on the high-resolution local earthquake tomography study of Improta et al. (2017) that merged and reprocessed all the data recorded by the different networks from 2002 to 2014 (Figure 1b). Apart from a natural background seismicity consisting of rare small swarms and sparse events occurring at 8–12 km depth at the base or underneath the Apulia Carbonate Platform, the seismicity clusters within the Apulian carbonate reservoir in two specific zones (Figures 1b and 1c): (a) to the southwest of the PWR where RIS has been documented since 2002 (Rinaldi et al., 2020; Stabile et al., 2015); (b) at the southeastern margin of the oilfield, where fluid injection induced microseismicity ($M \leq 2$) related the Costa Molina 2 disposal well, reactivated with an extensional kinematics a pre-existing thrust fault (Figures 1b and 1c) (Buttinelli et al., 2016; Hager et al., 2021; Improta et al., 2017). Natural and induced seismicity show prevailing NW-SE trending normal faulting mechanisms coherently with the orientation of mapped faults and of the SW-NE extensional stress field (SHmax is N120°–140°) constrained by borehole breakouts from deep wells of the oilfield (Cucci et al., 2004; Improta et al., 2017). Shear wave splitting analysis for stations of the 2005–2006 survey and of ENI monitoring network (Pastori et al., 2009, 2015) confirm breakouts stress data. In particular, the three stations closest to the RIS area show dominant fast polarization direction (i.e., SHmax directions) striking NW-SE to WNW-ESE and large values of the average lag-time (see Figure 2a).

3. Earthquake Data Analysis

We built an enhanced earthquake catalog of the PWR induced seismicity, with the aim of imaging the geometry of faults at depth, furnishing details of the seismicity pattern and investigating the seismicity statistical characteristics. First, we improved the precision of the high-quality earthquake catalog described in the paper by Improta et al. (2017); then, we use *TM* and double-difference methods to build up an enhanced high-resolution seismicity catalog.

3.1. Earthquake Catalogs

3.1.1. Initial Relocated Catalog

We re-analyzed the seismicity catalog from Improta et al. (2017), focusing our attention to the earthquakes located to the south-west of the PWR and interpreted as RIS. The starting data set is composed of 502 hand-picked earthquakes, recorded during the 13-month-long 2005–2006 temporary experiment, by a dense network of 45 seismic stations (the average receiver spacing is 5 km) composed by: 21 temporary 3C continuously-recording stations of the temporary experiment described in Valoroso et al. (2009), plus 24 permanent INGV and ENI stations, and accurately located in a 3D high-resolution V_P and V_P/V_S velocity model (Improta et al., 2017). To improve earthquake location quality, we first measured accurate CC delay times by using the time-domain CC function of Schaff and Waldhauser (2005). Then, we combined CC delay times with delay times computed from phase picks to compute high-precision relative locations using the double-difference (DD hereinafter) algorithm *hypoDD* (Waldhauser & Ellsworth, 2000; Waldhauser & Schaff, 2008). The final data set is composed of 502

high-precision earthquake locations defined, hereinafter, as the *initial-relocated-catalog* (Figure 2a). All details on the data processing are reported in Text S1 in Supporting Information S1.

3.1.2. Template-Matching Catalog

We applied the *k*-Means clustering algorithm (Lloyd, 1982) to the *initial-relocated-catalog*, to select 408 earthquakes used as *templates*. Then, we employed the open-source python-based TM detection algorithm *EqCorrScan* (Chamberlain et al., 2017) to the continuous data streams of the temporary network installed during 2005–2006. The application of the TM detection algorithm allowed us to extract a large number (about 27K) of new *detections* from the continuous data, having an averaged CC larger than 0.65. We computed *P*- and *S*-waves arrival times by using CC differential times between the *template* manually-picked arrival times and the new detections. We selected detections having at least 4 *P*- and 4 *S*-waves arrival times at 5 or more recording stations, in order to discard all the potential earthquakes with poor station coverage and insufficient number of *S*-wave arrivals to adequately constrain the hypocentral depth (Husen & Hardebeck, 2010). We computed absolute earthquake locations for the resulting 8,631 earthquakes, using a 1D ad-hoc *P*-wave velocity model (Improta et al., 2017) with the probabilistic non-linear location software *NonLinLoc* (Lomax et al., 2001). Almost all earthquakes (99%) have formal horizontal and vertical location errors lower than 1 km (Figure S1 in Supporting Information S1). Then, we run a large-scale double-difference relative location procedure using *P*- and *S*-wave relative arrival times (Waldhauser & Schaff, 2008). We obtained a final high-precision DD catalog composed of 5,070 events, referred hereinafter as the *TM-catalog* (Figure 2b). This catalog has formal hypocentral location uncertainties in the order of tens of meters (Figure S1 in Supporting Information S1). A complete description of data processing, application of the TM algorithm and data selection is reported in Text S2 in Supporting Information S1. We show an example of a M_L −0.10 earthquake detected from a M_L 0.9 *template* in Figure S2 in Supporting Information S1.

3.2. Frequency Magnitude Distribution and *b-Value* Estimation

We estimated M_L for the new *TM-catalog* (Figure S3 in Supporting Information S1) and computed the FMD parameters for both *initial-relocated-catalog* and *TM-catalog*. We calculated the completeness magnitude M_C by following the *Goodness-of-Fit* technique (Wiemer & Wyss, 2000), while we estimated the *b-value* using the maximum-likelihood estimator of Aki (1965), and its uncertainty following the Shi and Bolt (1982) and the bootstrap methods (Text S4 and Figure S4 in Supporting Information S1).

According to our estimates, the *initial-relocated-catalog* has $M_C = 0.6$ and *b-value* $= 0.92 \pm 0.04$. These values are in agreement with those ($M_C = 0.4$ and *b-value* $= 0.88 \pm 0.02$) obtained by Chiaraluce et al. (2009) for almost the same earthquake catalog, with small variations due to catalog size and methods. The FMD for the whole *TM-catalog* reports a minimum $M_C = 0.2$ and *b-value* $= 1.19$ with an uncertainty of ± 0.03 (Figure S4 in Supporting Information S1). We benefited from the high-resolution of the *TM-catalog* to investigate the spatial distribution of the *b-value* (Section 4.2 and Text S4 in Supporting Information S1).

4. Results

The new *TM-catalog* consists of 5,070 earthquakes. The M_C reduction with respect to the *initial-relocated-catalog* is equal to 0.4 (Figure S4 in Supporting Information S1). Similar works using TM detection techniques report M_C reductions up to 1 unit of magnitude (e.g., Ross et al., 2019). In our case, the lower value is probably due to the already low M_C of the *initial-relocated-catalog* depending on the dense seismic network geometry, the overall low level of the ambient noise in the region, and the careful setting of the input parameters for the STA/LTA detection algorithm (Valoroso et al., 2009).

4.1. Seismicity Pattern

High-precision locations for both the *initial-relocated-catalog* and *TM-catalog* (Figure 2) help reconstruct spatiotemporal seismicity distribution in detail. This allows us to investigate the relationship between seismicity and water level changes in the Pertusillo lake and provides a reliable picture of the complex network of activated faults, exposing previously unknown fault segments.

The space-time distribution of the *initial-relocated-catalog* (Figure 2a) clearly shows that seismicity is organized in four distinct clusters, suggesting the progressive southward activation of *C1–C4*. Magenta-violet dots (days

0–60 of the experiment) mostly occur close to the PWR, while it is evident a change through greenish to reddish dots (day 260–420 of the experiment) away from the reservoir. The significantly larger number of events of the *TM-catalog* hampers the use of the color-coded palette as in Figure 2a; thus, we indicate the four clusters with four different colors (Figure 2b) while we describe their temporal distribution in detail in Figure 3. Here, we separate the contribution of each cluster and we plot diagrams showing the seismic rate (3-day-bins histogram), the cumulative number of events and the occurrence of $M > 1.5$ earthquakes.

To investigate the relationship between the water storage variations and the seismic release, we compare the four plots with the water level in the PWR starting from May 2005 (blue curve in Figure 3a). The water level curve shows an evident seasonal oscillation. A continuous decrease during fall-winter 2005 (A–B in Figure 3a) is followed by a rapid increase from November 2005 to January 2006 (B–C). After a break of about 40 days (C–D), the refill phase continues up to March 2006 when the highest level is reached (E). The water level remains at high values until mid-May 2006 (F), then it starts decreasing to reach the minimum value in November. During the fall-winter rapid refill phase, the lake level change reaches the large value of 14 m, which corresponds to a significant variation in the reservoir storage of about 74 million m^3 (i.e., about half of the maximum reservoir storage of 155 million m^3).

The number of events progressively decreases during the emptying phase (days 0–200 of the experiment) and abruptly increases following the rapid refill phase (around day 240). All diagrams remark a clear relation of the seismic rate with the lake level change: low-seismicity during the initial unloading phase (around days 1–90); very low seismic release when the lake level is low (days 90–210); increasing (days 210–270) and high seismic release (days 270–390) during the loading phase and when the water column is high. A similar annual trend characterizes the other episodes of intense seismicity monitored by sparser permanent stations (years 2003, 2004, 2013, and 2014 in Figure 1d): high seismicity rates relate to high reservoir levels during the winter-spring stage, and vice-versa. Such a correlation is supported by statistical analysis of the long-term (2002–2012) PWR seismicity (Telesca et al., 2015).

The four clusters share the same general trend of increasing seismic rate following the rapid fall-winter refill phase (day 200), suggesting that all clusters can be interpreted in terms of RIS. However, there are significant differences. While the initial increase of seismicity that follows the refill phase is gradual for all clusters, C2, C3, and C4 are characterized by bursts of seismicity and by a main peak of activity during spring 2006 (see numbered arrows in Figure 3). The peak of activity is not simultaneous but it shows a delayed activation from *C2–C4* (i.e., day 312 for *C2*; 348 for *C3*; and 366 for *C4*). In terms of number of earthquakes, *C2* is the most productive, followed by *C3*, *C4*, and *C1*. Conversely, in terms of energy release, *C3* is associated with the largest number (11) $M \geq 1.5$ events and by the occurrence of the two strongest events ($M > 2.5$), while *C2* and *C4* have four and seven $M \geq 1.5$ earthquakes, respectively. We show a detailed map and cross-section view of the *initial-relocated-catalog* and enhanced *TM-catalog* for the four clusters in Figures 4 and 5. To better define the geometry of the activated faults, we select 4,084 highly correlated earthquakes out of the total 5,070 whole *TM-catalog*, whose hypocentral locations are well-constrained by at least 200 *P*-waves and 200 *S*-waves delay times. These events represent 80% of the whole *TM-catalog*. To illustrate the kinematics of the activated faults we show 86 focal mechanism solutions computed by Improta et al. (2017) for the best located earthquakes ($M_L > 1$ and at least 8 *P*-wave first motion polarities) and tracing the rays in the 3D tomographic model. Fifty earthquakes (58%) have normal faulting kinematics (gray beach balls in Figures 4 and 5). The remaining events have either strike-slip (orange, 18 events for 21%) or transtensive kinematics (green, 18 events for 21%). Further details on the computation of the focal mechanisms are reported in Improta et al. (2017). We did not compute additional focal mechanisms for this paper, due to the very small magnitude of the newly detected events.

For each cluster, we describe the spatial seismicity distribution and kinematics.

Cluster 1 (C1): is the closest to the PWR. It extends for ~4-km along strike (N110°E direction) between 1.5 and 5.5 km depth. *Initial-relocated-catalog* seismicity occurs in two small spots, without highlighting any fault (sections 1–4 in Figure 4). Toward the Pertusillo lake, the enhanced *TM-catalog* (green dots) shows distributed seismicity that elongates between 3 and 5.5 km depth highlighting a NW-striking SW-dipping high-angle structure. This latter is associated with a M_L2 earthquake at its base (section 7 in Figure 4). To the SW, a zone of diffuse seismicity develops between 1 and 5 km depth (sections 7–8). An isolated spot of seismicity is evident at the northwestern termination of the cluster, associated with a $M_L1.7$ event (section 5). The few larger events have mostly normal faulting kinematics with NW-SE trending nodal planes.

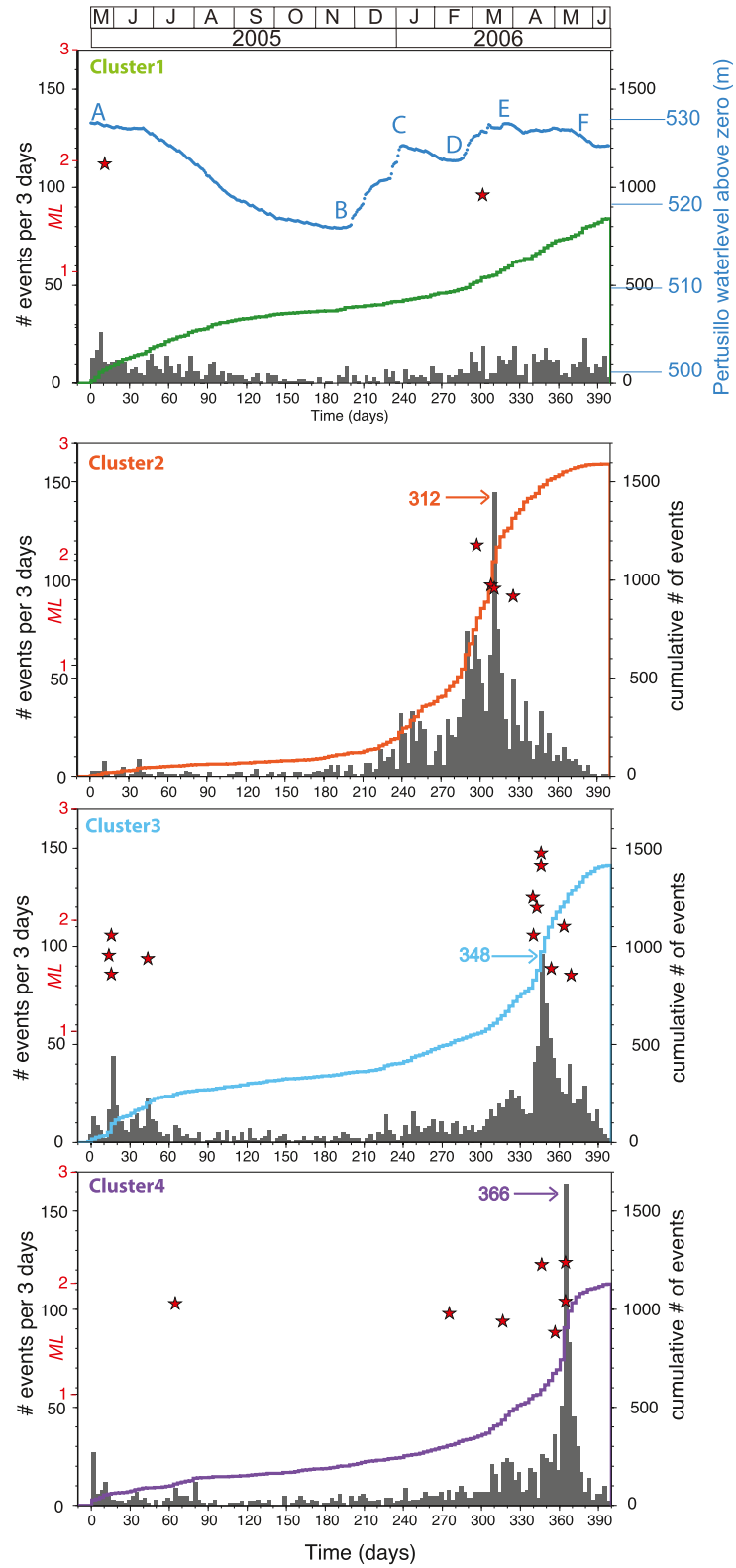

Figure 3. Histograms showing the number of events with time (3-day-bin) for each seismicity cluster. Solid lines represent the cumulative number of events versus time. Red stars are $M_L \geq 1.5$ earthquakes. For each cluster, numbered arrows outline the main peak of seismicity (see text for explanation). *The top histogram also shows the water level in the Pertusillo water reservoir* (*data are from* http://www.adb.basilicata.it/adb/ente.asp *and are shown in meters above sea level*).

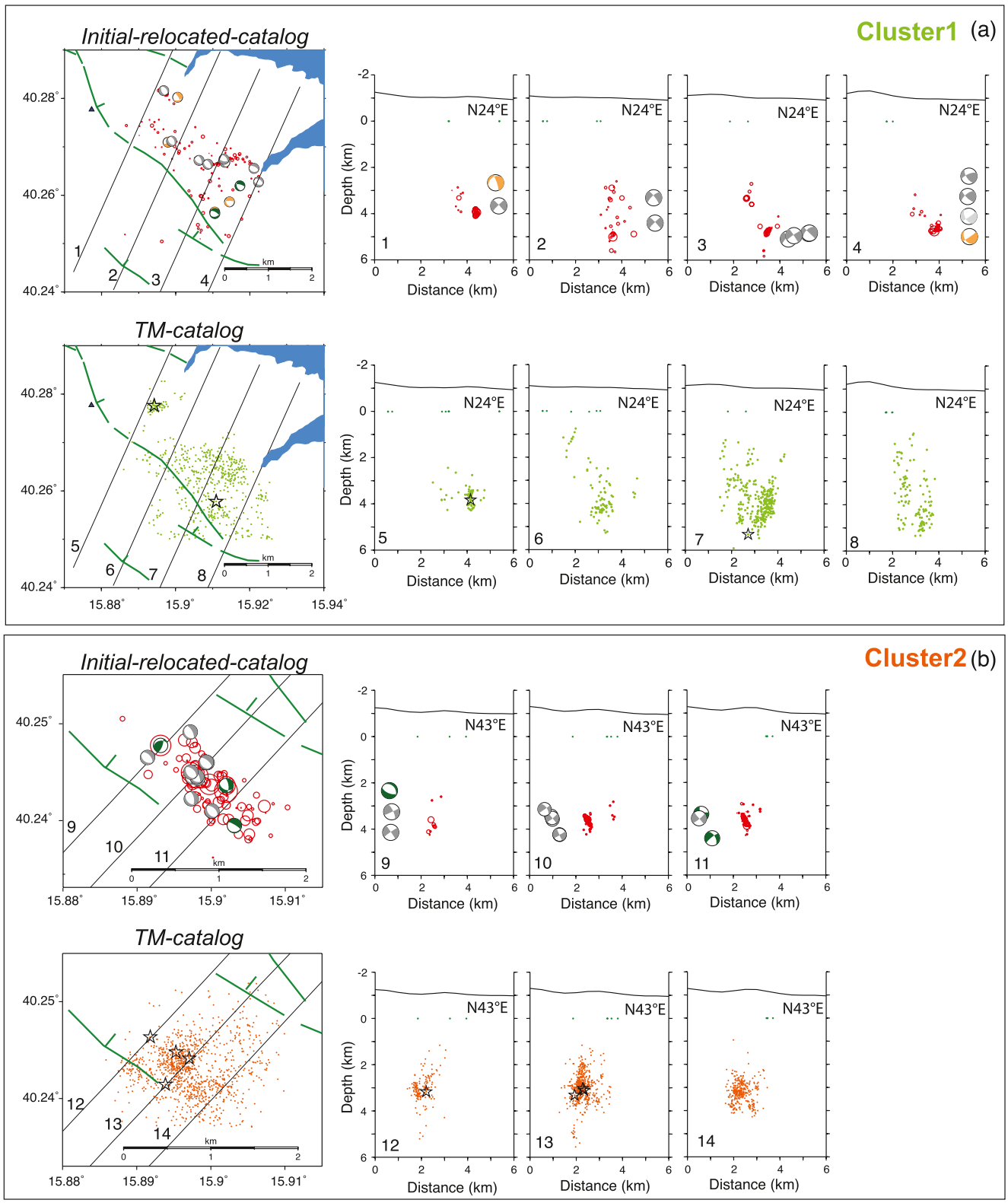

Figure 4. Detailed map and cross-section view of Cluster1 (panel *a*) and Cluster2 (panel *b*) seismicity. Cross-sections are spaced 500 m. For each cluster, the top panel shows the *initial-relocated-catalog* (red circles, whose size indicates the approximate source dimension, assuming a 3 MPa circular constant stress drop source) along with focal mechanism solutions for $M_L > 1$ earthquakes. Gray, green and orange beach balls indicate normal, transtensive or strike-slip kinematics. The bottom panel shows 4,084 highly correlated earthquakes of the *TM-catalog* (see text for explanation), with green (C1) and orange (C2) dots. Stars indicate $M_L \geq 1.5$ earthquakes.

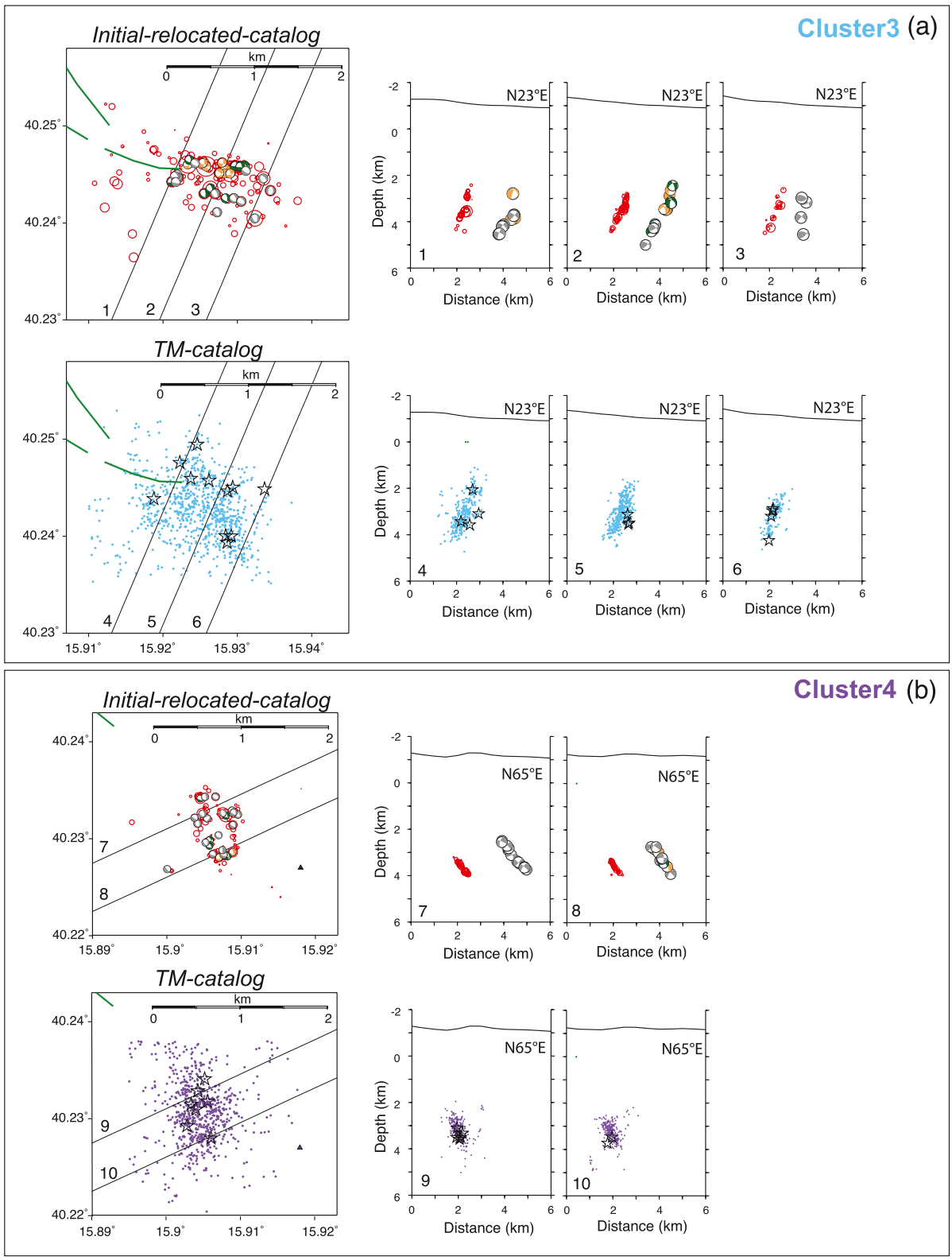

Figure 5. Detailed map and cross-section view of Cluster3 (panel *a*) and Cluster4 (panel *b*). The description is the same reported for Figure 4.

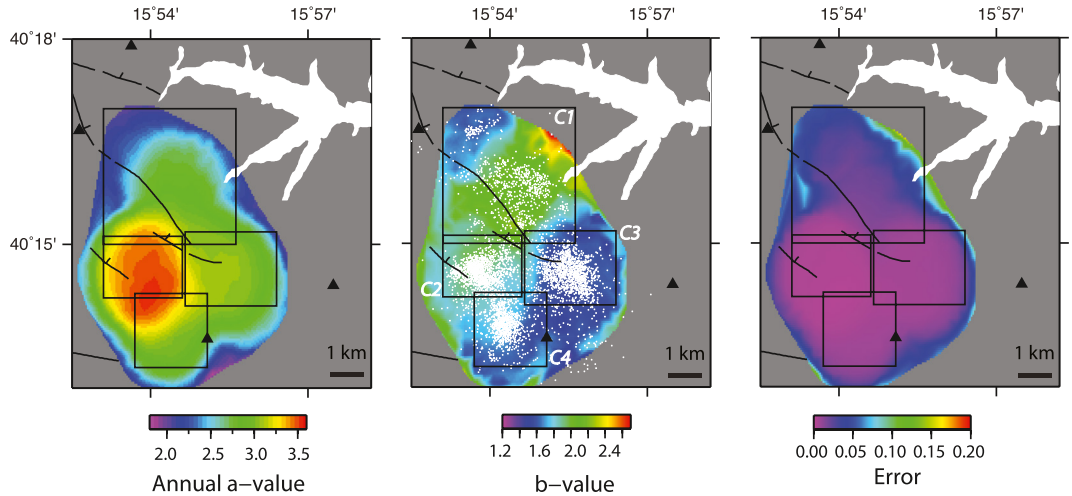

Figure 6. The figure shows: (a) annual *a-value*, (b) *b-value* of the frequency-magnitude distribution. (c) Error in the estimation of the *b-value*, computed from 5,000 bootstrap resampling of each *1-km-radius* circular cell (see text and Figure S7 in Supporting Information S1).

Cluster 2 (C2): extends for ∼1.5 km along-strike (N130°E direction) between 1.5 and 4 km depth. *Initial-relocated-catalog* defines a clear small plane that steeply dips to NE between 3.3 and 4 km depth (sections 9–11 in Figure 4). *TM-catalog* shows a broader volume of seismicity between 2 and 4 km depth; within this volume, small alignments of events define a more complex network of oppositely dipping minor steep faults (sections 12–14). Focal mechanism solutions are prevailing normal faulting, coherent with the high-angle NE-dipping fault.

Cluster 3 (C3): extends for ∼2.5 km along strike (N110°E direction) between 1 and 4.5 km depth (Figure 5). Most events of the *TM-catalog* align along a clear NW-trending, SW-dipping high-angle fault that measures 4 km along dip. Such structure is illuminated only in part by the *initial-relocated-catalog* (sections 1–3). All the eleven $M_L > 1.5$ events occur along this fault. At a closer look, the fault is structured into two segments: a shallower (<3.5 km depth) sub-vertical segment with prevailing E-W trending strike-slip focal solutions (section 2 of the *initial-relocated-catalog* and section 5 of the *TM-catalog*) and a deeper segment (75° to SW) with NW-trending extensional focal mechanisms.

Cluster 4 (C4): The *TM-catalog* defines a clear NNW-trending (N160°E) plane, dipping 55° to the NE (sections 7–10 in Figure 5). This fault, ∼2-km-long along-strike and defined between 2.5 and 4 km depth, is pictured by the *initial-relocated-catalog* only for 0.8 km along strike and between 3.5 and 4 km in depth. Also in this case, all the largest events (seven $M_L > 1.5$) occur along the fault. The focal mechanisms show prevailing normal faulting solutions in good agreement with the hypocenter alignments.

4.2. *b-Value* Distribution

We used the enhanced *TM-catalog* to investigate variations of the *b-value* of the FMD among the individual clusters. The completeness magnitude of the four sub-catalogs varies between $M_C = 0.1$ for *C3* and *C4* to $M_C = 0.3$ for *C2*. *b-value* varies between 1.19 and 1.54 (Figure S5 in Supporting Information S1).

We selected events with $M_L \geq 0.4$, the largest spatially observed M_C (Figure S6 in Supporting Information S1), to compute the *b-value* spatial distribution with the aim of investigating whether the four clusters displayed different characteristics that could give insights into their physical properties. We are aware that accurate estimates of the *b-value* parameter of the FMD are often hampered by the intrinsic uneven distribution of the seismicity in space and time, making the computation of this parameter a delicate issue (e.g., Marzocchi et al., 2020; van der Elst, 2021 and reference therein). Taking this in mind, we carefully tested the dimensions of the circular cells used for the computation, as well as the minimum number of events to validate the measurements within each single 1.5-km-radius cell. Details of the procedure used to calculate the spatial pattern of *b-value* (Figure 6) are reported in Text S4 and Figures S6–S8 in Supporting Information S1.

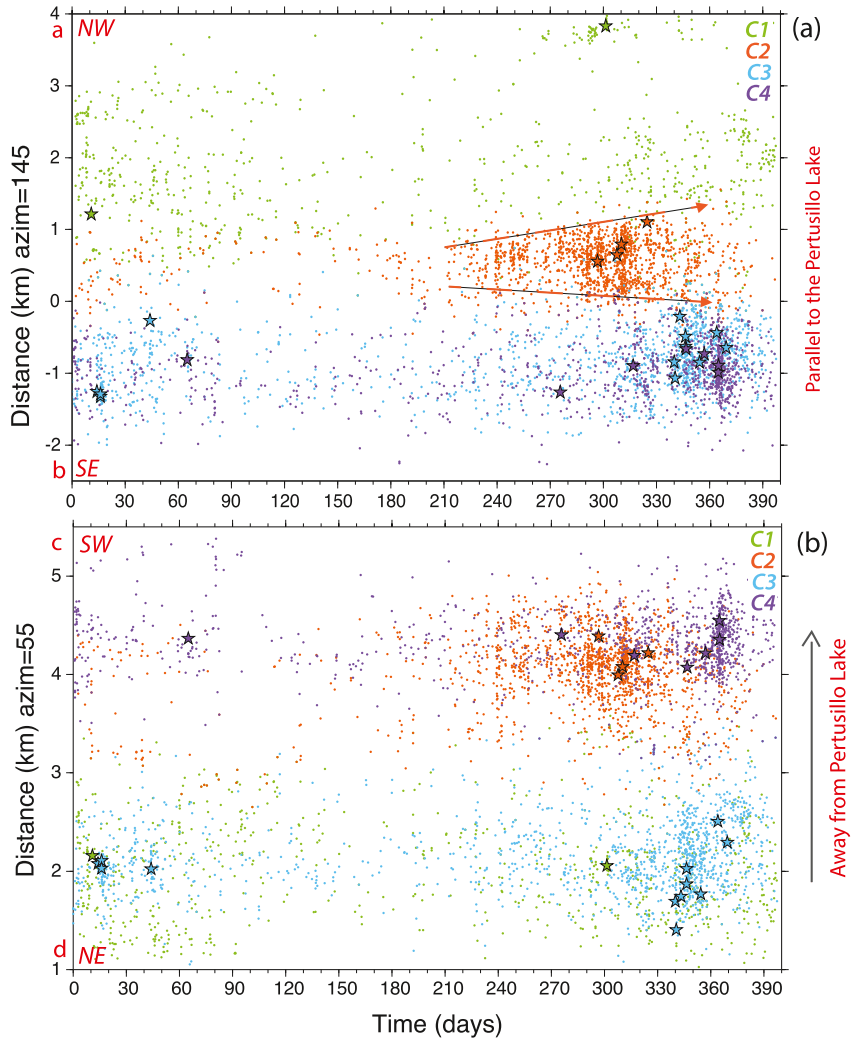

Figure 7. Two diagrams showing the spatiotemporal seismicity distribution projected along two orthogonal vertical cross-sections (black lines in Figure 2b). (a) Seismicity projected along a 6.5-km-long N145°E trending vertical section following the general trend of the four clusters (a–b line in Figure 2b); (b) Seismicity projected along a 4.5-km-long section (N55°E) orthogonal to the Pertusillo (c–d line in Figure 2b). Orange dashed lines in diagram (a) outline the very slow bilateral expansion of the *C2* seismicity. Green, orange, light-blue and violet dots are for *C1–C4* seismicity.

In map view, the *b-value* defines two main zones (Figure 6b): large to very large values (1.6–2) in the northwestern sector and relatively low values (around 1.3) in the southeastern one (see also Figure S8 in Supporting Information S1). High *b-value* volumes enclose clusters *C1* and partially *C2*, while low *b-value* volumes enclose *C3* and *C4*. We underline that larger *b-value* characterizes the northwestern volume of distributed seismicity (*C1* and partially *C2*), whereas lower *b-value* characterizes southeastern volume (*C3* and *C4*) where seismicity clusters along fault planes and includes (relatively) larger earthquakes (Figures 4 and 5 for details).

4.3. Space-Time Seismicity Diagrams

We investigate possible preferential directions of migration of the seismicity by using space-time diagrams, obtained by projecting hypocentral locations on two vertical sections (Figure 7). Among different directions tested to highlight seismicity migration, we chose two directions (black lines in Figure 2b): (a) a 6.5-km-long NW-striking section (N145°) (Figure 7a) and (b) a 4.5-km-long orthogonal section (N55°E) aimed at illustrating possible seismicity migration away from the PWR (Figure 7b). We use these diagrams to investigate the seismicity migration velocity and to check whether the seismicity distribution showed a triggering-front parabolic envelope, typical of fluid-induced triggering mechanisms (i.e., Shapiro et al., 2003).

Both diagrams confirm that *C1* seismicity is almost randomly distributed in space and time (Figure 7a) while *C3* and *C4* share a strong space-time clustering of both $M \geq 1.5$ shocks and lower magnitude seismicity, testified by the light blue and violet earthquake vertical alignments in Figure 7b. *C2* shows a light slow bilateral NW-SE-trending migration (orange arrows in Figure 7a), whereas *C1*, *C3*, or *C4* do not show clear migration directions. The subtle expansion of the *C2* swarm since day 210 accounts for a very small velocity of 3 m/day that we measured using a simple linear fit shown with orange arrows in Figure 7a. Interestingly, this low migration velocity coexists with repeated episodes of high seismic release (seismic bursts) lasting for a very short time (<1 day), characterized by exceptionally fast migration velocity in the order of km/day (i.e., orange vertical stripes in Figure 7), separated by more quiescent phases. These bursts activate multiple minor faults of *C2* (cross-sections 12–14 in Figure 4). A similar seismicity pattern characterizes *C4* during the main peak of activity (violet dots in Figure 7).

The space-time diagrams confirm the lack of clear hypocenter spreading from the Pertusillo reservoir to the RIS area. In addition, a pressure diffusion model does not fit the short seismic-bursts with velocity in the order of km/day or the very slow expansion of the *C2* swarm, with migration velocities of 3–6 m/day. These low velocities would imply exceptionally low hydraulic diffusivity, in contrast with the high permeability of the Apulian fractured carbonate reservoir (k in the order of 10^{-13}–10^{-15} m^2; Improta et al., 2017).

5. Discussion

We processed 13-month of continuous data from a dense temporary experiment in the Val d'Agri area by combining *TM* and *double-difference* methods. We first computed high precision double-difference relative locations for the *initial-relocated-catalog* and we used 408 selected earthquakes as *templates*. Then, we obtained a new high-precision *TM-catalog* of 5,070 earthquakes significantly larger than the *initial-relocated-catalog* processed with standard (STA-LTA) detection methods. Both catalogs allowed us to better reconstruct the seismicity pattern, the fault architecture and to investigate spatial changes in the *b-value* parameter of the FMD, fostering a better interpretation of the activated structures with respect to previous studies.

In the following sections, we will discuss our results in comparison with subsurface geological models and other seismological observables such as Vp and Vp/Vs tomographic models of the area. We aim at investigating how physical and hydraulic properties of the subsurface influence the seismicity distribution, allowing us to better interpret the observed space-time seismicity distribution and to give insights on the PWR seismicity.

5.1. Pre-Existing Subsurface Structure Control on the RIS Distribution

Previous works (Improta et al., 2017; Stabile et al., 2014) interpreted the PWR induced seismicity as due to the activation of the Monti della Maddalena NE-dipping normal-fault system, based on the seismicity spatial distribution and kinematics (Figure 1). Field geologic data and shallow geophysical surveys show that this fault system is composed of NW-SE trending active fault-splays dipping around 60° to the NE (Improta et al., 2010; Maschio et al., 2005). Faults illuminated by the *TM-catalog* do not reconcile with these seismotectonic interpretations. Instead, we provide evidence of a complex architecture of blind faults with opposite dipping directions (NE- and SW-dipping), higher dip angles (from 65° to subvertical) and with strike directions that are oblique to the Monti della Maddalena fault system, as for the *C4* NNW-SSE fault (strike N155°–160°, *C4* in Figure 5). In particular, we note that the largest illuminated fault (*C3*) dips to the SW, in contrast with the NE-dipping geometry of the Monti della Maddalena fault segments.

These findings spur a revision of the subsurface structure to investigate the relationship between RIS and geological structures. We compare the high-precision *TM-catalog* with a structural model the Inner Apulian Platform constrained by subsurface data (La Bruna et al., 2018; Nicolai & Gambini, 2007) and with Vp and Vp/Vs tomographic models of the Apulian reservoir (Improta et al., 2017). The former give constraints on the morphology of the top of the Apulian carbonates and on the geometry/kinematics of faults dissecting the carbonates (Figure 8a), the latter give insights into the physical properties of the Apulian aqueous reservoir (lithology, fracturing, pore-fluid pressure). The tomographic models are parametrized by a 2×1 km node spacing horizontally and vertically, respectively, and well resolved down to 5 km depth. High-precision earthquake locations are projected onto the 3-km-depth horizontal layer and two vertical sections in Figures 8b and 8c.

To the southwest of PWR, the Apulian carbonates are deformed by the broad ramp anticline of the Castellana Trend (Pugliese et al., 2011) developed during the Late Pliocene-Early Pleistocene contractional phase

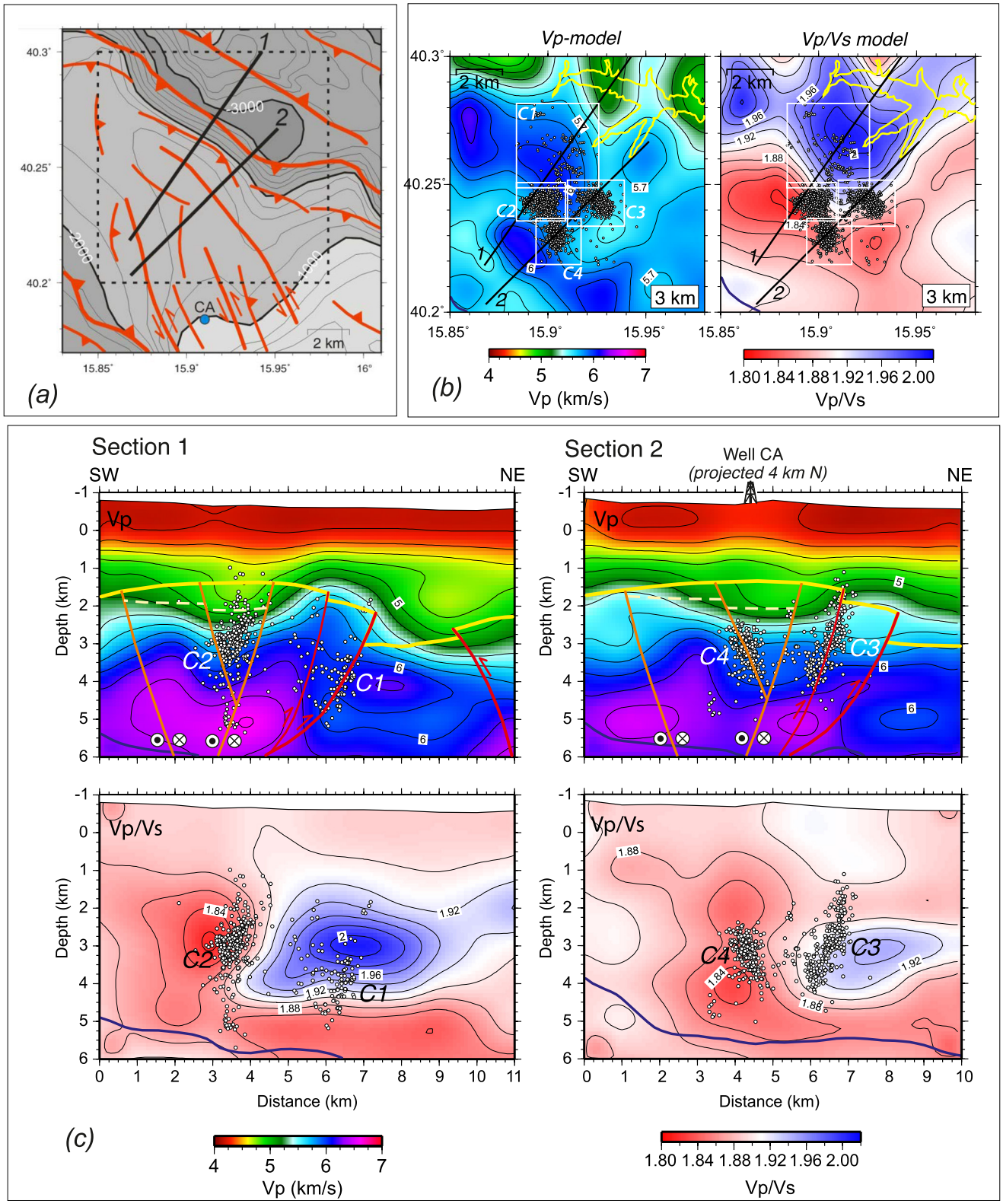

Figure 8.

(Figure 8a). This structure relates to a main blind thrust fault reported by Nicolai and Gambini (2007) that strikes NW-SE and steeply dips to the southwest. The top of the Apulian carbonates is deeper than 3 km (b.s.l.) in the fault footwall and rapidly rises to about 1.4 km depth along the fold crest (Figure 8a). The frontal thrust has a clear signature in the tomographic model (section 1 in Figure 8c): the footwall block corresponds to an evident low-Vp anomaly (Vp < 5 km/s), while the fold forelimb corresponds to a high-Vp bump elongated in the NW-SE direction with Vp values typical of fractured Cretaceous-Miocene limestones (Vp = 5.6–6.0 km/s; Improta et al., 2017). Below 4 km depth, the frontal thrust marks an evident lateral heterogeneity, with Vp increasing from 6.0 to 6.5 km/s, that we interpret as very-high velocity Jurassic-Triassic dolomites of the Apulia Platform (see Improta et al., 2014, 2017; Trippetta et al., 2010) tectonically juxtaposed above the limestones.

Under the crest of the ramp anticline, the Apulia Platform is characterized by anomalous Vp values of 4.8–5.4 km/s that define a velocity sag (Figure 8c). Seismic reflection profiles and deep well data document a considerable thickening of Messinian coarse-grained turbidites that stratigraphically cover the shelf limestone in this area (Finetti et al., 2005; La Bruna et al., 2018; Van Dijk et al., 2000). The Messinian clastic sequence has thickness >600 m, low Vp values around 4.5–5.0 km/s, and was interpreted as the infill of a foreland basin developed during the southward flexure of the Apulia Platform, in response to the hinge-retreat of the Adria plate (La Bruna et al., 2018). The basin development was controlled by a set of conjugate high-angle extensional faults, reactivated as transpressive sinistral faults striking NW-SE (Figure 8a and orange lines in Figure 8c) during the Late Pliocene—Early Pleistocene compressive phase (La Bruna et al., 2018; Mazzoli et al., 2014; Van Dijk et al., 2000). We therefore interpret the low-Vp sag at the top of the Apulia Platform to represent the fault-controlled Messinian basin reported by La Bruna et al. (2018) (the basin is defined schematically by a dashed yellow line in Figure 8c).

The Vp/Vs model gives further insights into the physical properties of the Apulian carbonates. An anomalous region of very-high Vp/Vs (up to 2.02) encompasses the frontal thrust and the anticline forelimb (Figure 8b and section 1 in Figure 8c). We interpret this region as a zone of diffuse deformation, where a pervasive network of fractures and small faults is associated with the thrust activity. The exceptionally high Vp/Vs also indicates brine-saturated carbonates with high fracture permeability. This interpretation agrees with the strong crustal anisotropy found in this area by Pastori et al. (2009, 2015), with dominant fast polarization direction striking from WNW-ESE to NW-SE and large values of the average lag-time (Figure 2a).

Relatively low Vp/Vs (1.82–1.88) characterize instead the southern sector, which corresponds to the anticline backlimb, and the deep part of the Apulia Platform (>4 km depth). The remarkable lateral Vp/Vs variation trends NW-SE (Figure 8b) and has values that increase rapidly from 1.82 to 2.02 over a 3-km distance range (section 1 in Figure 8c). Such relatively low Vp/Vs, which coexist with high Vp in the 6.0–6.4 km/s range, likely reflects a change in the physical and hydraulic properties of the carbonates, presumably related to a less pervasive network of fractures and small faults away from the main thrust fault of the Castellana Trend.

The PWR seismicity is almost exclusively located within the Apulian carbonates and clearly relates to inherited faults of the Castellana Trend (Figure 8). Cluster *C1* is within the very-high-Vp/Vs region. The strip of distributed seismicity, striking NW-SE and dipping SW, can be related to the frontal thrust (section 1 in Figure 8c). The diffuse and shallower seismicity, that is evident in the 3-km-depth layer, is confined in the forelimb of the ramp anticline. The absence of clear event alignments (i.e., on-fault seismicity) is consistent with the hypothesis of diffuse rock-fracturing affecting this strongly deformed sector of the Apulia Platform.

The subvertical cluster *C2* develops in the anticline backlimb and matches the low-Vp structure related to the fault-controlled Messinian basin (section 1 in Figure 8c). The earthquake distribution suggests a link with the

Figure 8. (a) Structural map of the top of the Inner Apulian Platform in the study area. The contour map is based on: (a) the regional structural model of the Apulian Platform of Nicolai and Gambini (2007) modified with some local data (Improta et al., 2017; and references therein); (b) the subsurface models of La Bruna et al. (2018) for the southern sector. The blue circle denotes the Castellana 1 (CA) well. Black lines indicate the two vertical cross-sections shown in panel (c). (b) Vp and Vp/Vs depth slices (2–5 km depth) in the study area extracted from the high-resolution local earthquake tomography model of Improta et al. (2017). The thick blue line delimits the well-resolved sector of the model with values of the (Spread Function < 2). White dots are double-difference relative locations of the *TM-catalog*. Black rectangles delimit the four seismicity clusters. (c) Earthquake hypocenters projected on two Vp and Vp/Vs sections (section 1 includes clusters 1–2, section 2 clusters 3–4). Main structures of the Inner Apulia Platform are schematically reported on the velocity cross-sections. The top of the Apulian unit (yellow line) is extracted from the top contour map shown in panel (a). Position, dip and kinematics of the Apulian structures are constrained by: (a) the structural model of Nicolai and Gambini (2007) for Late Pliocene reverse faults (red lines), (b) data of La Bruna et al. (2018) and Van Dijk et al. (2000) for the Messinian foreland-basin faults reactivated with sinistral strike-slip kinematics during Early Pleistocene (orange lines). The dashed yellow line schematically represents the bottom of the Messinian foreland basin constrained by the CA well and corresponding to low-Vp velocities. The thick blue lines delimit well-resolved regions (Spread Function <2.0) of the velocity model. Earthquakes are projected within ±250 m distance from the sections.

inherited basin-bounding fault system: its NW-SE trend is coherent with the faults strike, while seismicity seems to delineate a system of oppositely dipping minor faults (Figure 4) that mimics the conjugate steep faults imaged by seismic reflection profiles (La Bruna et al., 2018). *C2* bounds to the SW the very-high Vp/Vs anomaly and the hypocenter distribution follows the strong lateral Vp/Vs heterogeneity.

Both *C3* and *C4* clearly relate to blind faults cutting the Apulian carbonates. The *C3* on-fault seismicity matches a subsidiary reverse fault that splays from the frontal thrust (section 2 in Figure 8c). This provides compelling evidence of re-activation and tectonic inversion of an inherited NW-striking thrust fault favorably oriented for failure in the NE-SW extensional stress field. In the earthquake zone, Vp/Vs weakly decreases from 1.92 to 1.86 toward the south (Figure 8b). *C3* seismicity dies out in correspondence with the top of the Apulian carbonates, tightening RIS nucleation to the physical properties of the reservoir and seal rocks. Coherently to what reported by Improta et al. (2017) for fluid-injection induced seismicity, we reckon that seismic slip above the Apulian limestones is inhibited by the ductile rheology of the cap-rock clayey formation.

The *C4* on-fault seismicity matches a structure that may belong to the Messinian basin-bounding system (section 2 in Figure 8c). This interpretation is also supported by the NNW-SSE orientation of *C4* that is coherent with the rotation of the Apulian transpressive structures from NW-SE to NNW-SSE in the southern region (Figure 8a). *C4* seismicity is located within a zone of relatively low Vp/Vs (1.84–1.86) (Figures 8b and 8c).

5.2. Rock Physical Properties and *b-Value* Distribution

Numerous studies report a wide range of *b-values* worldwide, highlighting its relationship with tectonic stress (Amorèse et al., 2010; Schorlemmer et al., 2005). In general, high *b-value* characterize lower-magnitude (i.e., small size ruptures) sparse seismicity associated to diffuse fracture networks, while low *b-value* are observed along well-developed faults where larger patches can slip seismically. Also, low *b-value* pinpoints highly stressed portions of the crust such as fault asperities, as reported for the 2009 L'Aquila sequence (De Gori et al., 2012; Gulia et al., 2016; Sugan et al., 2014), the 2012 Pollino swarms (Passarelli et al., 2015) in the Apennine belt, as well as during other foreshock-aftershock sequences worldwide (Gulia and Wiemer, 2009; Van der Elst, 2021). The same behavior has been observed during laboratory experiments showing a systematic *b-value* decrease when the stress increases before main slipping events (e.g., Goebel et al., 2012) or during hydraulic fracturing underground experiments (De Barros et al., 2016; Villiger et al., 2020).

In a recent paper on the 2016 Mw6.5 Central Italy sequence, Collettini et al. (2022) reports on the key role played by the lithology and rheological behavior of carbonate rocks, similar to those of the Apulian units, in the space-time distribution and *b-value* of aftershocks. The authors found that on-fault low-*b-value* seismicity correlates to zones of localized brittle deformation associated with large normal faults. Conversely, off-fault high-*b-value* distributed seismicity correlates to zones of diffuse deformation characterized by widespread networks of fractures and small faults.

Our survey unravels significant spatial variations of the *b-value* (Figure 6): a high *b-value* region (>1.6) encloses clusters *C1* and partially *C2*, while areas of relatively low *b-value* (around 1.2) enclose *C3* and *C4*. We observe a general correlation between the spatial pattern of *b-value*, Vp/Vs heterogeneities and seismicity distribution, suggesting a key role of rock physical properties in controlling the PWR seismicity.

In the northwestern region, high to very-high *b-values* (>1.6) coexist with high Vp/Vs and distributed seismicity (Figure 8b). This reconciles with the interpretation proposed in the previous section for *C1*: seismicity spreads in a zone of diffuse deformation characterized by a pervasive network of distributed fractures and small faults developed in the anticline forelimb and related to hundred-of-meters-thick fault zones (red lines in Figure 8c). The activation of distributed faults and fractures is likely favored by high pore fluid pressure in the fractured carbonates, as suggested by the very-high Vp/Vs (up to 2).

In the southeastern region, lower *b-values* (about 1.2) and Vp/Vs (1.8–1.9) characterize the *C3* and *C4* on-fault seismicity (Figures 8b and 8c) that illuminates km-scale pre-existing faults of the Apulian thrust-belt. Larger events ($M_L > 2.0$) rupture asperities with source dimensions in the order of 100–400 m (Zoback & Gorelick, 2012), reflecting localized rock fracturing along major faults in the Apulian carbonates. *C2* shows an intermediate behavior with respect to the end-members *C1* and *C3–C4*. Seismicity spreads over a region wherein both the *b-value* and Vp/Vs rapidly increase northeastward (Figures 6, 8b, and 8c). Such a variability is consistent with

the complex seismicity pattern that suggests the re-activation of minor faults within well-developed fracture networks.

5.3. Driving Mechanism of the Pertusillo Reservoir Induced Seismicity

The physical mechanism underlying the Pertusillo RIS is still not well understood. Water level variations in a lake produce volumetric and shear deformations that can affect the hydraulic and mechanical properties of the rock volume and induce pore-fluid pressure transients, modulating seismicity rates (Talwani, 1997; Gupta, 2022; among others).

To date, three main physical mechanisms have been proposed in literature for anthropogenic induced seismicity (Schultz et al., 2020 and reference therein). The first simpler mechanism is related to pore-fluid pressure increase and diffusion through conductive pathways. The increase of pore-fluid pressure reduces the effective normal stress along faults or fractures until they reach the point of failure. This mechanism requires a direct hydraulic connection between the source of pressure perturbations and the volume where seismicity takes place. As examples, protracted RIS associated with the Itoiz water reservoir (Spain) developed in karst terranes has been interpreted as directly triggered by fluid diffusion within high-permeability fault-zones (Dura-Gomez & Talwani, 2010), while the initial seismicity linked to the giant Three Gorges Reservoir in China has been related to water infiltration through major faults and fractured carbonates (Zhou et al., 2017). A clear example of RIS migrating along a fault is reported for the Acu reservoir (Brazil) by El Hariri et al. (2010). Based on accurate locations of weak events, these authors were able to pinpoint location of a shallow fault that acts as an effective fluid pathway underneath the reservoir and to infer fracture permeability through hydraulic diffusivity modeling.

The second mechanism is based on the poroelastic stress transmission model (e.g., Segall & Lu, 2015) in which seismicity is triggered by means of a coupled effect of pore pressure and elastic stress increase in the rock fabric. This mechanism does not require a direct hydraulic connection between the source region and the area where seismicity develops, accounting for seismicity rate changes away from the artificial lake and/or where fluid diffusion is inhibited by low permeability rock volumes. Poroelasticity has been used to model seismicity rate changes due to water reservoir loading or level changes (e.g., Kusalara & Talwani, 1992; Reoloffs, 1988; Rinaldi et al., 2020) and to suggest a clock-advance triggering effect for the 2008 Mw7.9 Wenchuan earthquake (China), located 12 km from the Zipingpu reservoir (Tao et al., 2015).

The third mechanism invokes a combination of poroelastic stress and aseismic slip, accounting for numerous observations reporting imbricated seismic and aseismic deformation released along fluid pressurized fractures and faults (e.g., Cornet et al., 1997; Guglielmi et al., 2015; De Barros et al., 2020; Eyre et al., 2020). This mechanism has never been invoked for RIS so far.

The joint interpretation of all data shown in this paper, that is, seismicity pattern, *b-value*, structural and velocity models, furnish us hints to improve understanding of the mechanisms underlying the Pertusillo RIS. Our data rule out the first hypothesis based on pore-fluid pressure diffusion along conductive pathways. Indeed, there is no evidence of seismicity migration compatible with fluid pressure diffusion along pathways connecting the PWR and the zones where RIS takes place, nor along the single blind faults illuminated by event alignments (Section 4.3). Besides, the pile of low-permeability clayey and siliciclastic sequences at different structural levels (Hager et al., 2021; La Bruna et al., 2018) below the PWR hinders the existence of effective hydraulic pathways that could connect the lake floor to the RIS volume.

Our observations point to a more complex physical mechanism underlying the RIS explained by a delayed poroelastic stress change due to the significant gravitational loading/unloading phases that progressively involves the strongly fractured and brine-saturated Apulian carbonates. The delayed and progressive activation of the seismicity clusters away from the lake agrees with a mechanism of propagation of strain and stress changes away from the source of gravitational load. The spatial distribution of the resulting stress is influenced by local variations in physical and hydraulic properties of the carbonate reservoir. Low *b-value* seismicity re-activates inherited faults favorably oriented for slip in the present-day extensional stress field, breaking earthquake-prone fault asperities (*C3* and C4), whereas high *b-value* seismicity relates to pervasive fracture networks developed within brine-saturated carbonates characterized by high Vp/Vs (*C1* and partially *C2*). These observations agree with the recent poroelastic modeling of Rinaldi et al. (2020) that well explains the long-term PWR seismicity in terms of poroelastic deformation associated with seasonal variations of the reservoir storage. According to their model,

the seasonal level variations of the lake can produce an increase in Coulomb failure stress of 0.05–0.5 bar in the source volume of RIS for NW-SE trending faults with extensional kinematics, hence comparable to those identified in our study. Such stress values are larger than those proposed for triggering seismicity, from both natural or anthropogenic sources, that is, earth tides, groundwater recharge of large karst aquifers or anthropogenic sources (Cochran et al., 2004; D'Agostino et al., 2018; Keranen et al., 2014; among others).

In addition to the proposed driving mechanism, we recognize possible evidence of aseismic slip deformation in triggering part of the seismicity. Indeed, the observed seismicity distribution is often organized in vertical stripes alternating fast seismic bursts that do not follow a diffusive behavior (i.e., orange and violet stripes in Figure 7), with more quiescent phases. Following recent works (De Barros et al., 2020, 2021; Fischer & Hainzl, 2021), these fast-growing streak episodes might indicate aseismic slip episodes along high-critically stressed faults. We speculate that these aseismic episodes, followed by earthquake-earthquake interactions, might be a plausible interpretation for the PWR seismicity, reactivating well-developed fault-zones of large, inherited thrust faults within the fluid-saturated Apulian carbonates.

Our results confirm the importance of mapping the complex interaction among stress changes caused by human activity, pre-existing faults and local stress field in the assessment of the hazard posed by the induced seismicity. In this perspective, we provide key information for detailed geomechanical modeling of the Coulomb stress changes associated with the gravitational lake loading/unloading on the newly accurately defined optimally oriented faults.

A final observation regards the mounting evidence suggesting that crustal microseismicity can be modulated by significant seasonal changes in continental groundwater storage (Johnson et al., 2017; among others). For the Pertusillo related seismicity, we can exclude the contribution of possible large karst aquifers hosted in thick platform carbonate sequences that could trigger seasonal microseismicity, as observed in the Campania Apennines (D'Agostino et al., 2018) or eastern Alps (Pintori et al., 2021). Platform carbonate thrust sheets do not outcrop where the Pertusillo RIS takes place but to the NW and SE (Figure 1a). In addition, the carbonate units have a limited extension and/or thickness that could not host large karst aquifers as those investigated by D'Agostino et al. (2018) and Pintori et al. (2021).

As a final comment, we acknowledge that our study is based on a short-time-window (i.e., 13-month-long) dense passive survey. Unfortunately, longer time-window catalogs, that is, the 2001–2014 revised catalog of Improta et al. (2017), use data from sparse monitoring stations resulting in a seismic catalog characterized by completeness magnitude and location accuracy, not adequate to perform high-resolution analysis of the long-term seismicity. Additional studies covering more seasonal loading/unloading reservoir cycles can be carried out in the future by using a recently installed seismic local network (Stabile et al., 2020).

6. Conclusions

We computed a high-precision enhanced earthquake catalog of the Pertusillo lake RIS by using *TM* and double-difference methods. The new *TM-catalog* consists of 5,070 events, a 10-fold increase with respect to the *initial-relocated-catalog*. The combined interpretation of the spatiotemporal seismicity pattern, the *b-value* spatial distribution, together with geological and seismic tomography models of the upper crust allowed us to reconstruct the geometry of the activated faults and to give insights into the physical and hydraulic properties of the rock volume where RIS takes place.

Our main conclusions can be summarized as follow:

1. Seismicity is organized in four distinct clusters, showing a progressive southward activation in response to loading/unloading phases of the Pertusillo reservoir. Almost all earthquakes nucleate within the fractured Apulian aqueous carbonate reservoir. Distributed seismicity relates to pervasive fracture networks, whereas on-fault seismicity re-activates and invert reverse and transpressive faults of the Late Pliocene-Early Pleistocene shortening phase. These faults are favorably oriented to slip in the present-day extensional stress regime. The newly imaged km-scale fault segments were missing or only partially illuminated by previously available seismic catalogs. Thus, our results provide key insights about the complex fault system activated by RIS.
2. We do not find clues of a link between the faults illuminated by RIS and the Monti della Maddalena extensional fault system (Figure 1), quoted as the main seismogenic structure of the region by some authors (Burrato

& Valensise, 2008; among others). Investigating the relationship between this exposed normal-fault system and the inherited blind thrust faults within the Apulian carbonates would require a careful re-interpretation of seismic commercial profiles (proprietary), which is not the aim of this paper. Nevertheless, earthquakes define a complex, about 8-km-long fault system that clearly represents a potential source of moderate earthquakes (e.g., the *C3* fault has a source dimension of 4-km along-dip and 2-km along-strike corresponding to earthquakes in the range $M = 3.8–4.5$ (Zoback & Gorelick, 2012)).

3. The spatial distribution of the *b-value* presents significant variations, with values ranging from 1.2 to 2.2, that we relate to the physical properties of the Apulian carbonate reservoir (rock fracturing, pore-fluid pressure). A region of high- to very-high *b-value* (>1.6) and distributed seismicity reasonably map volumes of diffuse deformation, where pervasive networks of fractures and small faults develop in brine-saturated carbonates (i.e., the very-high Vp/Vs zone). On the contrary, (relatively) low *b-value* (1.2) points to zones of localized "on-fault" deformation characterized by low Vp/Vs. Here, low-magnitude seismicity and (relatively) larger events ($M_L > 2$) collapse along pre-existing km-scale steep-dipping faults, rupturing critically stressed fault asperities (e.g., Gulia & Wiemer, 2019; among others).
4. We shed light on the primary role exerted by the pre-existing fault structure, stress field and physical/hydraulic properties of the Apulian carbonates on the seismic release, giving valuable information on the physical mechanism behind the RIS. The blind faults illuminated by RIS have experienced multi-phase deformation and currently slip with extensional kinematics in response to stress perturbations induced by the seasonal variations of the water reservoir storage. We therefore speculate that fracture network characteristics control the seismicity behavior (i.e., *b-value*) as observed for hydrofracturing/hydroshear laboratory tests and aftershock sequences (Collettini et al., 2022; Goebel et al., 2017; Villiger et al., 2020; among others).
5. The space-time earthquake migration is not compatible with a fluid diffusion mechanism along permeable pathways (i.e., faults) connecting directly the lake with the RIS volume. All observations suggest that a poroelastic stress transmission mechanism is the most suitable to explain the Pertusillo induced seismicity in agreement with other RIS case studies (Reoloffs, 1988). We also recognize interesting seismicity patterns, that is, fast-growing streak episodes suggesting aseismic slip episodes along high-critically stressed faults (De Barros et al., 2020, 2021; Fischer & Hainzl, 2021).

Our results confirm the importance of understanding the complex interaction among stress changes caused by human activity, pre-existing faults and local stress field in the assessment of the hazard posed by the induced seismicity. In this perspective, our study yields key information for future geomechanical modeling of the Coulomb stress changes associated with the gravitational lake loading/unloading.

Conflict of Interest

The authors declare no conflicts of interest relevant to this study.

Acknowledgments
This work has been supported within the PRIN-MUSE-4D project of the Italian PRIN-MIUR program (Grant 2017KT2MKE). Preliminary locations of the *initial-relocated-catalog* were developed within the 2018 Master Thesis by Karola Schultz (Universitat Potsdam). Some plots were made with the Generic Mapping Tools v.4.2.1 (www.soest.hawaii.edu/gmt; Wessel & Smith, 1998). L.I. thanks Vincenzo La Bruna and Fabrizio Agosta (University of Basilicata) for useful discussions on the Apulia inherited structures. L.V. and D.P. are grateful to Pasquale De Gori for discussions about the *b-value* computation and spatial distribution interpretation. The authors would like to thank the editor, the associate editor and two anonymous reviewers for their comments and suggestions that have helped us improve the final manuscript.

Data Availability Statement

The *template-matching* earthquake catalog is available at: https://doi.org/10.5281/zenodo.7951142 (Valoroso et al., 2023b). Continuous seismic data of the Val d'Agri temporary network (Federation of Digital Seismograph Networks [FDSN] network identifier X6) are described and available here: https://doi.org/10.13127/SD/F705_MAIX3 (Valoroso et al., 2023a). Water reservoir data are available at http://www.adb.basilicata.it/adb/ente.asp.

References

Aki, K. (1965). Maximum likelihood estimate of bin the formula logN=a−bm and its confidence limits. *Bulletin of the Earthquake Research Institute, University of Tokyo*, *43*, 237–238.

Amitrano, D. (2003). Brittle-ductile transition and associated seismicity: Experimental and numerical studies and relationship with the *b-value*. *Journal of Geophysical Research*, *108*(B1), 1–15. https://doi.org/10.1029/2001jb000680

Amorèse, D., Grasso, J. R., & Rydelek, P. A. (2010). On varying *b-values* with depth: Results from computer-intensive tests for Southern California. *Geophysical Journal International*, *180*(1), 347–360. https://doi.org/10.1111/j.1365-246X.2009.04414.x

Bello, S., Lavecchia, G., Andrenacci, C., Ercoli, M., Cirillo, D., Carboni, F., et al. (2022). Complex trans-ridge normal faults controlling large earthquakes. *Scientific Reports*, *12*(1), 10676. https://doi.org/10.1038/s41598-022-14406-4

Burrato, P., & Valensise, G. (2008). Rise and fall of a hypothesized seismic gap: Source complexity in the Mw 7.0 16 December 1857 southern Italy earthquake. *Bulletin of the Seismological Society of America*, *98*(1), 139–148. https://doi.org/10.1785/0120070094

Buttinelli, M., Improta, L., Bagh, S., & Chiarabba, C. (2016). Inversion of inherited thrusts by wastewater injection induced seismicity at the Val d'Agri oilfield (Italy). *Scientific Reports*, *6*(1), 37165. https://doi.org/10.1038/srep37165

Candela, S., Mazzoli, S., Megna, A., & Santini, S. (2015). Finite element modelling of stress field perturbations and interseismic crustal deformation in the Val d'Agri region, southern Apennines, Italy. *Tectonophysics*, *657*, 245–259. https://doi.org/10.1016/j.tecto.2015.07.011

Cello, G., Tondi, E., Micarelli, L., & Mattioni, L. (2003). Active tectonics and earthquake sources in the epicentral area of the 1857 Basilicata earthquake (southern Italy). *Journal of Geodynamics*, *36*(1–2), 37–50. https://doi.org/10.1016/S0264-3707(03)00037-1

Chamberlain, C. J., Hopp, C. J., Boese, C. M., Warren-Smith, E., Chambers, D., Chu, S. X., et al. (2017). EQcorrscan: Repeating and near-repeating earthquake detection and analysis in Python. *Seismological Research Letters*, *89*(1), 173–181. https://doi.org/10.1785/0220170151

Chiaraluce, L., Valoroso, L., Anselmi, M., Bagh, S., & Chiarabba, C. (2009). A decade of passive seismic monitoring experiments with local networks in four Italian regions. *Tectonophysics*, *476*(1–2), 85–98. https://doi.org/10.1016/j.tecto.2009.02.013

Cochran, E. S., Ross, Z. E., Harrington, R. M., Dougherty, S. L., & Rubinstein, J. L. (2018). Induced earthquake families reveal distinctive evolutionary patterns near disposal wells. *Journal of Geophysical Research: Solid Earth*, *123*(9), 8045–8055. https://doi.org/10.1029/2018JB016270

Cochran, E. S., Vidale, J. E., & Tanaka, S. (2004). Earth tides can trigger shallow thrust fault earthquakes. *Science*, *306*(5699), 1164–1166. https://doi.org/10.1126/science.1103961

Collettini, C., Barchi, M. R., De Paola, N., Trippetta, F., & Tinti, E. (2022). Rock and fault rheology explain differences between on fault and distributed seismicity. *Nature Communications*, *13*(1), 1–11. https://doi.org/10.1038/s41467-022-33373-y

Cornet, F. H., Helm, J., Poitrenaud, H., & Etchecopar, A. (1997). Seismic and aseismic slips induced by larger-scale fluid injections. *Pure and Applied Geophysics*, *150*(3–4), 563–583. https://doi.org/10.1007/s000240050093

Cucci, L., Pondrelli, S., Frepoli, A., Mariucci, M. T., & Moro, M. (2004). Local pattern of stress field and seismogenic sources in the Pergola-Melandro basin and the Agri valley (Southern Italy). *Geophysical Journal International*, *156*(3), 575–583. https://doi.org/10.1111/j.1365-246X.2004.02161.x

D'Adda, P., Longoni, R., Magistroni, C., Meda, M., Righetti, F., Cavozzi, C., et al. (2018). Extensional reactivation of a deep transpressional architecture: Insights from sandbox analogue modeling applied to the Val d'Agri basin (southern Apennines, Italy). *Interpretation*, *5*(1), SD55e66. https://doi.org/10.1190/INT-2016-0078.1

D'Agostino, N., Silverii, F., Amoroso, O., Convertito, V., Fiorillo, F., Ventafridda, G., & Zollo, A. (2018). Crustal deformation and seismicity modulated by groundwater recharge of karst aquifers. *Geophysical Research Letters*, *45*(22), 12253–12262. https://doi.org/10.1029/2018GL079794

De Barros, L., Cappa, F., Deschamps, A., & Dublanchet, P. (2020). Imbricated aseismic slip and fluid diffusion drive a seismic swarm in the Corinth Gulf, Greece. *Geophysical Research Letters*, *47*(9), e2020GL087142. https://doi.org/10.1029/2020GL087142

De Barros, L., Daniel, G., Guglielmi, Y., Rivet, D., Caron, H., Payre, X., et al. (2016). Fault structure, stress, or pressure control of the seismicity in shale? Insights from a controlled experiment of fluid-induced fault reactivation. *Journal of Geophysical Research: Solid Earth*, *121*(6), 4506–4522. https://doi.org/10.1002/2015JB012633

De Barros, L., Wynants-Morel, N., Cappa, F., & Danr, P. (2021). Migration of fluid-induced seismicity reveals the seismogenic state of faults. *Journal of Geophysical Research: Solid Earth*, *126*(11), e2021JB022767. https://doi.org/10.1029/2021JB022767

De Gori, P., Lucente, F. P., Lombardi, A. M., Chiarabba, C., & Montuori, C. (2012). Heterogeneities along the 2009 L'Aquila normal fault inferred by the *b*-value distribution. *Geophysical Research Letters*, *39*(15), L15304. https://doi.org/10.1029/2012GL052822

DISS Working Group. (2010). Retrieved from http://diss.rm.ingv.it/diss/. https://doi.org/10.6092/INGV.IT-DISS3.1.1

Dura-Gomez, I., & Talwani, P. (2010). Hydromechanics of the Koyna-Warna region India. *Pure and Applied Geophysics*, *167*(1–2), 183–213. https://doi.org/10.1007/s00024-009-0012-5

El Hariri, M., Abercrombie, R. E., Rowe, C. A., & do Nascimento, A. F. (2010). The role of fluids in triggering earthquakes: Observations from reservoir induced seismicity in Brazil. *Geophysical Journal International*, *181*, 1566–1574. https://doi.org/10.1111/j.1365-246X.2010.04554.x

Eyre, T. S., Zecevic, M., Salvage, R. O., & Eaton, D. W. (2020). A long-lived swarm of hydraulic fracturing-induced seismicity provides evidence for aseismic slip. *Bulletin of the Seismological Society of America*, *110*(5), 2205–2215. https://doi.org/10.1785/0120200107

Ferranti, L., Palano, M., Cannavò, F., Mazzella, M. E., Oldow, J. S., Gueguen, E., et al. (2014). Rates of geodetic deformation across active faults in southern Italy. *Tectonophysics*, *621*, 101–122. https://doi.org/10.1016/j.tecto.2014.02.007

Finetti, I. R., Lentini, F., Carbone, S., Del Ben, A., Di Stefano, A., Guarnieri, P., et al. (2005). Crustal tectono-stratigraphy and geodynamics of the Southern Apennines from CROP and other integrated geophysical-geological data. In I. R. Finetti (Ed.), *CROP PROJECT: Deep seismic exploration of the Central Mediterranean and Italy*. Elsevier Publishing.

Fischer, T., & Hainzl, S. (2021). The growth of earthquake clusters. *Frontiers in Earth Science*, *9*, 638336. https://doi.org/10.3389/feart.2021.638336

Goebel, T. H. W., Becker, T. W., Schorlemmer, D., Stanchits, S., Sammis, C., Rybacki, E., & Dresen, G. (2012). Identifying fault heterogeneity through mapping spatial anomalies in acoustic emission statistics. *Journal of Geophysical Research*, *117*(B3), B03310. https://doi.org/10.1029/2011JB008763

Goebel, T. H. W., Kwiatek, G., Becker, T. W., Brodsky, E. E., & Dresen, G. (2017). What allows seismic events to grow big?: Insights from *b*-value and fault roughness analysis in laboratory stick-slip experiments. *Geology*, *45*(9), 815–818. https://doi.org/10.1130/G39147.1

Guglielmi, Y., Cappa, F., Avouac, J.-P., Henry, P., & Elsworth, D. (2015). Seismicity triggered by fluid injection-induced aseismic slip. *Science*, *348*(6240), 1224–1226. https://doi.org/10.1126/science.aab0476

Gulia, L., Tormann, T., Wiemer, S., Herrmann, M., & Seif, S. (2016). Short-term probabilistic earthquake risk assessment considering time-dependent *b-values*. *Geophysical Research Letters*, *43*(3), 1100–1108. https://doi.org/10.1002/2015gl066686

Gulia, L., & Wiemer, S. (2019). Real-time discrimination of earthquake foreshocks and aftershocks. *Nature*, *574*(7777), 193–199. https://doi.org/10.1038/s41586-019-1606-4

Gupta, H. K. (2022). Artificial water reservoir-triggered seismicity (RTS): Most prominent anthropogenic seismicity. *Surveys in Geophysics*, *43*(2), 619–659. https://doi.org/10.1007/s10712-021-09675-z

Hager, B. H., Dieterich, J., Frohlich, C., Juanes, R., Mantica, S., Shaw, J. H., et al. (2021). A process-based approach to understanding and managing triggered seismicity. *Nature*, *595*(7869), 684–689. https://doi.org/10.1038/s41586-021-03668-z

Husen, S., & Hardebeck, J. L. (2010). *Earthquake location accuracy*. Community Online Resource for Statistical Seismicity Analysis. https://doi.org/10.5078/corssa-55815573

Improta, L., Bagh, S., De Gori, P., Valoroso, L., Pastori, M., Piccinini, D., et al. (2017). Reservoir structure and wastewater-induced seismicity at the Val d'Agri oilfield (Italy) shown by three dimensional V_p and V_p/V_s local earthquake tomography. *Journal of Geophysical Research: Solid Earth*, *122*(11), 9050–9082. https://doi.org/10.1002/2017JB014725

Improta, L., De Gori, P., & Chiarabba, C. (2014). New insights into crustal structure, Cenozoic magmatism, CO_2 degassing, and seismogenesis in the southern Apennines and Irpinia region from local earthquake tomography. *Journal of Geophysical Research: Solid Earth*, *119*(11), 8283–8311. https://doi.org/10.1002/2013JB010890

Improta, L., Ferranti, L., De Martini, P. M., Piscitelli, S., Bruno, P. P., Burrato, P., et al. (2010). Detecting young, slow-slipping active faults by geologic and multidisciplinary high-resolution geophysical investigations: A case study from the Apennine seismic belt, Italy. *Journal of Geophysical Research*, *115*(B11), B11307. https://doi.org/10.1029/2010JB000871

Improta, L., Valoroso, L., Piccinini, D., & Chiarabba, C. (2015). A detailed analysis of wastewater induced seismicity in the Val d'Agri oil field (Italy). *Geophysical Research Letters*, *42*(8), 2682–2690. https://doi.org/10.1002/2015GL063369

Johnson, C. W., Fu, Y., & Burgmann, R. (2017). Seasonal water storage, stress modulation, and California seismicity. *Science*, *356*(6343), 1161–1164. https://doi.org/10.1126/science.aak9547

Keranen, K. M., Weingarten, M., Abers, G. A., Bekins, B. A., & Ge, S. (2014). Sharp increase in central Oklahoma seismicity since 2008 induced by massive wastewater injection. *Science*, *345*(6195), 448–451. https://doi.org/10.1126/science.1255802

Kusalara, J., & Talwani, P. (1992). The role of elastic, undrained, and drained responses in triggering earthquakes at Monticello Reservoir, South Carolina. *Bulletin of the Seismological Society of America*, *82*(4), 1867–1888. https://doi.org/10.1785/bssa0820041867

La Bruna, V., Agosta, F., Lamarche, J., Viseur, S., & Prosser, G. (2018). Fault growth mechanisms and scaling properties in the foreland basin system: The case study of Monte Alpi, Southern Apennines, Italy. *Journal of Structural Geology*, *116*, 94–113. https://doi.org/10.1016/j.jsg.2018.08.009

Lloyd, S. P. (1982). Least squares quantization in PCM. *IEEE Transactions on Information Theory*, *28*(2), 129–137. https://doi.org/10.1109/tit.1982.1056489

Lomax, A., Zollo, A., Capuano, P., & Virieux, J. (2001). Precise, absolute earthquake location under Somma-Vesuvius volcano using a new 3D velocity model. *Geophysical Journal International*, *146*(2), 313–331. https://doi.org/10.1046/j.0956-540x.2001.01444.x

Mallet, R. (1862). *Great Neapolitan earthquake of 1857 - The first principles of observational seismology*. Chapman & Hall.

Marzocchi, W., Spassiani, I., Stallone, A., & Taroni, M. (2020). How to be fooled searching for significant variations of the *b-value*. *Geophysical Journal International*, *220*(3), 1845–1856. https://doi.org/10.1093/gji/ggz541

Maschio, L., Ferranti, L., & Burrato, P. (2005). Active extension in Val d'Agri area, Southern Apennines, Italy: Implications for the geometry of seismogenic belts. *Geophysical Journal International*, *162*(2), 591–609. https://doi.org/10.1111/j.1365-246X.2005.02597.x

Mazzoli, S., Ascione, A., Buscher, J. T., Pignalosa, A., Valente, E., & Zattin, M. (2014). Low-angle normal faulting and focused exhumation associated with late Pliocene change in tectonic style in the southern Apennines (Italy). *Tectonics*, *33*(9), 1802–1818. https://doi.org/10.1002/2014tc003608

Mazzoli, S., Ascione, A., Candela, S., Iannace, A., Megna, A., Santini, S., & Vitale, S. (2013). Subduction and continental collision events in the southern Apennines: Constraints from two crustal cross-sections. *Rendiconti Online della Società Geologica Italiana*, *25*, 78–84. https://doi.org/10.3301/ROL.2013.07

Mazzoli, S., Barkham, S., Cello, G., Gambini, R., Mattioni, L., Shiner, P., & Tondi, E. (2001). Reconstruction of continental margin architecture deformed by the contraction of the Lagonegro Basin, southern Apennines, Italy. *Journal of the Geological Society*, *158*(2), 309–319. https://doi.org/10.1144/jgs.158.2.309

Nicolai, C., & Gambini, R. (2007). Structural architecture of the Adria platform-and-basin system. *Italian Journal of Geosciences*, *7*, 21–37. In A. Mazzotti, E. Patacca, & P. Scandone (Eds.), Results of the CROP project, sub-project CROP-04 Southern Apennines (Italy).

Passarelli, L., Hainzl, S., Cesca, S., Maccaferri, F., Mucciarelli, M., Roessler, D., et al. (2015). Aseismic transient driving the swarm-like seismic sequence in the Pollino range, Southern Italy. *Geophysical Journal International*, *201*(3), 1553–1567. https://doi.org/10.1093/gji/ggv111

Pastori, M., De Gori, P., Piccinini, D., Bagh, S., Improta, L., & Chiarabba, C. (2015). Induced seismicity from different sources in Italy: How to interpret it? In *Abstract S13B-2803 presented at 2015 fall meeting, 14–18 Dec*. AGU.

Pastori, M., Piccinini, D., Margheriti, L., Improta, L., Valoroso, L., Chiaraluce, L., & Chiarabba, C. (2009). Stress aligned cracks in the upper crust of the Val d'Agri region as revealed by shear wave splitting. *Geophysical Journal International*, *179*(1), 601–614. https://doi.org/10.1111/j.1365-246X.2009.04302.x

Patacca, E., & Scandone, P. (1989). Post-Tortonian mountain building in the Apennines: The role of the passive sinking of a relic lithospheric slab. In A. Boriani (Ed.), *The lithosphere in Italy, advances in Earth science research* (Vol. 80, pp. 157–176). Atti Conv. Lincei.

Pintori, F., Serpelloni, E., Longuevergne, L., Garcia, A., Faenza, L., D'Alberto, L., et al. (2021). Mechanical response of shallow crust to groundwater storage variations: Inferences from deformation and seismic observations in the eastern Southern Alps, Italy. *Journal of Geophysical Research: Solid Earth*, *126*(2), e2020JB020586. https://doi.org/10.1029/2020JB020586

Pugliese, A., Ghielmi, M., Barbacini, G., Carubelli, P., Magistroni, C., Miraglia, S., et al. (2011). Tertiary sedimentary and tectonic evolution of Apulian platform in the Val d'Agri subsurface area (Southern Italy). In *Extended abstract, AAPG international conference and exhibition, Milan, Italy, October 3–26, 2011*.

Reoloffs, E. A. (1988). Fault stability changes induced beneath a reservoir with cyclic variations in water level. *Journal of Geophysical Research*, *93*(B3), 2107–2124. https://doi.org/10.1029/JB093iB03p02107

Rinaldi, A. P., Improta, L., Hainzl, S., Catalli, F., Urpi, L., & Wiemer, S. (2020). Combined approach of poroelastic and earthquake nucleation applied to the reservoir-induced seismic activity in the Val d'Agri area, Italy. *Journal of Rock Mechanics and Geotechnical Engineering*, *12*(4), 802–810. https://doi.org/10.1016/j.jrmge.2020.04.003

Ross, Z. E., Trugman, D. T., Hauksson, E., & Shearer, P. M. (2019). Searching for hidden earthquakes in Southern California. *Science*, *364*(6442), 767–771. https://doi.org/10.1126/science.aaw6888

Rovida, A., & Antonucci, A. (2021). *EPICA - European PreInstrumental Earthquake CAtalogue, version 1.1*. Istituto Nazionale di Geofisica e Vulcanologia (INGV). https://doi.org/10.13127/epica.1.1

Schaff, D. P., & Waldhauser, F. (2005). Waveform cross-correlation-based differential travel-time measurements at the Northern California Seismic Network. *Bulletin of the Seismological Society of America*, *95*(6), 2446–2461. https://doi.org/10.1785/0120040221

Scholz, C. H. (2015). On the stress dependence of the earthquake *b-value*. *Geophysical Research Letters*, *42*(5), 1399–1402. https://doi.org/10.1002/2014GL062863

Schorlemmer, D., Wiemer, S., & Wyss, M. (2005). Variations in earthquake-size distribution across different stress regimes. *Nature*, *437*(7058), 539–542. https://doi.org/10.1038/nature04094

Schultz, R., Skoumal, R. J., Brudzinski, M. R., Eaton, D., Baptie, B., & Ellsworth, W. (2020). Hydraulic fracturing-induced seismicity. *Reviews of Geophysics*, *58*(3), e2019RG000695. https://doi.org/10.1029/2019RG000695

Segall, P., & Lu, S. (2015). Injection-induced seismicity: Poroelastic and earthquake nucleation effects. *Journal of Geophysical Research: Solid Earth*, *120*(7), 5082–5103. https://doi.org/10.1002/2015JB012060

Shapiro, S. A., Patzig, R., Rothert, E., & Rindshwentner, J. (2003). Triggering of seismicity by pore-pressure perturbations: Permeability-related signature of the phenomenon. *Pure and Applied Geophysics*, *160*(5–6), 1051–1066. https://doi.org/10.1007/pl00012560

Shearer, P. M. (1994). Global seismic event detection using a matched filter on long-period seismograms. *Journal of Geophysical Research*, *99*, 13–713. https://doi.org/10.1029/94JB00498

Shelly, D. R., Ellsworth, W. L., & Hill, D. P. (2016). Fluid-faulting evolution in high definition: Connecting fault structure and frequency-magnitude variations during the 2014 Long Valley caldera, California, earthquake swarm. *Journal of Geophysical Research: Solid Earth*, *121*(3), 1776–1795. https://doi.org/10.1002/2015jb012719

Shi, Y., & Bolt, B. (1982). The standard error of the magnitude-frequency *b* value. *Bulletin of the Seismological Society of America*, *72*(5), 1677–1687. https://doi.org/10.1785/bssa0720051677

Shiner, P., Beccaccini, A., & Mazzoli, S. (2004). Thin-skinned versus thick-skinned structural models for Apulian carbonate reservoirs: Constraints from the Val d'Agri Fields, S. Apennines, Italy. *Marine and Petroleum Geology*, *21*(7), 805–827. https://doi.org/10.1016/j.marpetgeo.2003.11.020

Spada, M., Tormann, T., Wiemer, S., & Enescu, B. (2013). Generic dependence of the frequency-size distribution of earthquakes on depth and its relation to the strength profile of the crust. *Geophysical Research Letters*, *40*(4), 709–714. https://doi.org/10.1029/2012GL054198

Stabile, T. A., Giocoli, A., Lapenna, V., Perrone, A., Piscitelli, S., & Telesca, L. (2014). Evidence of low magnitude continued reservoir-induced seismicity associated with the Pertusillo artificial lake (southern Italy). *Bulletin of the Seismological Society of America*, *104*(4), 1820–1828. https://doi.org/10.1785/0120130333

Stabile, T. A., Giocoli, A., Perrone, A., Piscitelli, S., Telesca, L., & Lapenna, V. (2015). Relationship between seismicity and water level of the Pertusillo reservoir (southern Italy). *Bollettino di Geofisica Teorica ed Applicata*, *56*(4), 505–517. https://doi.org/10.4430/bgta0161

Stabile, T. A., Serlenga, V., Satriano, C., Romanelli, M., Gueguen, E., Gallipoli, M. R., et al. (2020). The INSIEME seismic network: A research infrastructure for studying induced seismicity in the High Agri Valley (southern Italy). *Earth System Science Data*, *12*(1), 519–538. https://doi.org/10.5194/essd-12-519-2020

Sugan, M., Kato, A., Miyake, H., Nakagawa, S., & Vuan, A. (2014). The preparatory phase of the 2009 Mw 6.3 L'Aquila earthquake by improving the detection capability of low-magnitude foreshocks. *Geophysical Research Letters*, *41*(17), 6137–6144. https://doi.org/10.1002/2014GL061199

Talwani, P. (1997). On the nature of reservoir-induced seismicity. *Pure and Applied Geophysics*, *150*(3–4), 473–492. https://doi.org/10.1007/s000240050089

Tao, W., Masterlark, T., Shen, Z.-K., & Ronchin, E. (2015). Impoundment of the Zipingpu reservoir and triggering of the 2008 Mw 7.9 Wenchuan earthquake, China. *Journal of Geophysical Research: Solid Earth*, *120*(10), 7033–7047. https://doi.org/10.1002/2014JB011766

Telesca, L., Giocoli, A., Lapenna, V., & Stabile, T. A. (2015). Robust identification of periodic behavior in the time dynamics of short seismic series: The case of seismicity induced by Pertusillo Lake, southern Italy. *Stochastic Environmental Research and Risk Assessment*, *29*(5), 1437–1446. https://doi.org/10.1007/s00477-014-0980-6

Trippetta, F., Collettini, C., Vinciguerra, S., & Meredith, P. G. (2010). Laboratory measurements of the physical properties of Triassic Evaporites from Central Italy and correlation with geophysical data. *Tectonophysics*, *492*(1–4), 121–132. https://doi.org/10.1016/j.tecto.2010.06.001

Valoroso, L., Improta, L., Chiaraluce, L., Di Stefano, R., Ferranti, L., Govoni, A., & Chiarabba, C. (2009). Active faults and induced seismicity in the Val d'Agri area (Southern Apennines, Italy). *Geophysical Journal International*, *178*(1), 488–502. https://doi.org/10.1111/j.1365-246x.2009.04166.x

Valoroso, L., Improta, L., Piccinini, D., Chiarabba, C., Chiaraluce, L., Govoni, A., et al. (2023a). Seismic data acquired during the Val d'Agri temporary survey [Dataset]. Istituto Nazionale di Geofisica e Vulcanologia (INGV). https://doi.org/10.13127/SD/F705_MAIX3

Valoroso, L., Piccinini, D., Improta, L., & Gaviano, S. (2023b). Lake Pertusillo RIS catalog (Southern Italy) [Dataset]. Zenodo. https://doi.org/10.5281/zenodo.7951142

van der Elst, N. J. (2021). B-positive: A robust estimator of aftershock magnitude distribution in transiently incomplete catalogs. *Journal of Geophysical Research: Solid Earth*, *126*, e2020JB021027. https://doi.org/10.1029/2020JB021027

Van Dijk, J. P., Bello, M., Toscano, C., Bersani, A., & Nardon, S. (2000). Tectonic model and three-dimensional fracture network analysis of Monte Alpi (southern Apennines). *Tectonophysics*, *324*(4), 203–237. https://doi.org/10.1016/S0040-1951(00)00138-4

Villiger, L., Gischig, V. S., Doetsch, J., Krietsch, H., Dutler, N. O., Jalali, M., et al. (2020). Influence of reservoir geology on seismic response during decameter-scale hydraulic stimulations in crystalline rock. *Solid Earth*, *11*(2), 627–655. https://doi.org/10.5194/se-11-627-2020

Waldhauser, F., & Ellsworth, W. L. (2000). A double-difference earthquake location algorithm: Method and application to the northern Hayward Fault, California. *Bulletin of the Seismological Society of America*, *90*(6), 1353–1368. https://doi.org/10.1785/0120000006

Waldhauser, F., & Schaff, D. P. (2008). Large-scale relocation of two decades of Northern California seismicity using cross-correlation and double-difference methods. *Journal of Geophysical Research*, *113*(B8), B08311. https://doi.org/10.1029/2007JB005479

Wessel, P., & Smith, W. H. F. (1998). New, improved version of generic mapping tools released. *Eos, Transactions American Geophysical Union*, *79*(47), 579. https://doi.org/10.1029/98EO00426

Wiemer, S., & Wyss, M. (2000). Minimum magnitude of completeness in earthquake catalogs: Examples from Alaska, the Western United States, and Japan. *Bulletin of the Seismological Society of America*, *90*(4), 859–869. https://doi.org/10.1785/0119990114

Zhou, C., Yin, K., Cao, Y., Ahmed, B., Li, Y., Catani, F., & Pourghasemi, H. R. (2017). Landslide susceptibility modeling applying machine learning methods: A case study from Longju in the Three Gorges Reservoir area, China. *Computers & Geosciences*, *112*, 23–37. https://doi.org/10.1016/j.cageo.2017.11.019

Zoback, M. D., & Gorelick, S. M. (2012). Earthquake triggering and carbon sequestration. *Proceedings of the National Academy of Sciences*, *109*(26), 10164–10168. https://doi.org/10.1073/pnas.1202473109

References From the Supporting Information

Efron, B., & Tibshirani, R. J. (1994). *An introduction to the bootstrap* (1st ed.). Chapman and Hall/CRC. https://doi.org/10.1201/9780429246593

Keilis-Borok, V. I. (1959). An estimation of the displacement in an earthquake source and of source dimensions. *Annali di Geofisica*, *12*, 205–214.

Utsu, T. (1999). Representation and analysis of the earthquake size distribution: A historical review and some new approaches. *Pure and Applied Geophysics*, *155*(2–4), 509–535. https://doi.org/10.1007/s000240050276

Waldhauser, F. (2001). hypoDD: A program to compute double-difference hypocenter locations. U.S. Geol. Surv. Open File Rep., 01–113.